MEASUREMENT AND MODELING MILLIMETER-WAVE RESPONSE FROM SOIL SURFACES

Adib Y. Nashashibi
Fawwaz T. Ulaby
Kamal Sarabandi

ARO Contract: DAAL03-92-G-0269

Principal Investigator: Fawwaz T. Ulaby

September 1993

ABSTRACT

The millimeter-wave (MMW) backscatter response of bare-soil was examined by conducting experimental measurements at 35 and 94 GHz using a truck-mounted polarimetric scatterometer and by developing appropriate models to relate the backscattering coefficients to the soil's surface and volume properties. The experimental measurements were conducted for three soil surfaces with different roughnesses under both dry and wet conditions. The experimental measurements indicate that in general the backscattering coefficient is comprised of a surface scattering component σ^s and a volume scattering component σ^v. For wet soil conditions, the backscatter is dominated by surface scattering, while for dry conditions both surface and volume scattering are significant, particularly at 94 GHz. Because theoretical surface scattering models were found incapable of predicting the measured backscatter, a semi-empirical surface scattering model was developed that relates the surface scattering component of the total backscatter to the roughness parameter ks, where $k = 2\pi/\lambda$ and s is the rms height, and the dielectric constant of the soil surface. Volume scattering was modeled using radiative transfer theory with the packed soil particles acting as the host material and the air voids as the scattering particles. The combined contributions of surface and volume scattering was found to provide good agreement between the model calculations and the experimental observations.

Contents

List of Tables

List of Figures

1 INTRODUCTION

An extensive experimental investigation was conducted over the past three years to examine the polarimetric backscatter behavior of bare soil surfaces in the 1-10 GHz frequency range [1]. Using a set of truck mounted coherent polarimetric scatterometers with center frequencies at 1.25, 4.75 and 9.5 GHz, measurements were made of the Mueller matrix as a function of incidence angle for soil surfaces covering wide ranges of surface roughness and moisture content. Using the relations outlined in [1] and [2], the measured Mueller matrices were then used to compute the co-polarized backscattering coefficients σ^o_{vv} and σ^o_{hh}, the cross-polarized backscattering coefficient σ^o_{hv}, and the probability density functions of the co-polarized and cross-polarized phase differences. Comparison of the measured data with calculations based on the physical optics model, the geometric optics model, and the small perturbation method revealed that all three models are incapable of correctly predicting the backscatter response of random rough surfaces, even when applied within their presumed ranges of validity. This realization led Oh *et al.* [1] to develop a semi-empirical model that relates σ^o_{ij}, for $i,j = h\,or\,v$, to the incidence angle θ and the surface parameters ks and ϵ_r, where $k = 2\pi/\lambda$, s is the rms height and ϵ_r is the complex relative dielectric constant. The semi-empirical model, which was developed on the basis of measurements made during one season of experimental observations, was found to provide excellent agreement not only with observations made during two succeeding years for different sets of soil surfaces and conditions, but it also provided a reasonable match to experimental observations reported by Yamasaki *et al.* [3] for wet soil surfaces at 60 GHz.

This paper extends the preceding work by examining the backscatter response of soil surfaces at millimeter wavelengths (MMW), specifically 35 and 94 GHz. One of the major lessons learnt from the present study is that at 35 GHz and lower frequencies it is reasonable to assume that the backscatter from a half-space soil medium is due to scatter by the soil

surface alone, but at 94 GHz the backscatter consists of both surface and volume scattering contributions. Furthermore, for dry soils the volume-scattering component may be comparable to or greater than the surface-scattering component, but for wet soil the volume scattering component becomes negligibly small in comparison with the surface-scattering component. This behavior is consistent with calculations based on radiative transfer theory.

The next section contains detailed descriptions of the 35 and 94 GHz radar systems, the measurement procedure, and the measured properties of the soil surfaces. Section 3 provides an overview of the observed angular variation of σ^o for various surface roughnesses and introduces a scattering model composed of two terms, corresponding to surface and volume scattering contributions. The surface-scattering term is a semi-empirical expression that provides a better fit to the data than the expression previously derived by Oh *et al.* [1] for surface scattering at centimeter wavelengths. Section 4 examines the evidence for volume scattering and introduces a method for evaluating the volume-scattering term based on a numerical solution of the radiative transfer equation for a medium in which the soil particles are considered to be the host material and the air voids are the scatterers.

2 EXPERIMENTAL SETUP

The first part of this section provides a brief discription of the polarimetric scatterometers used in support of the present study. It is then followed with discussions of the techniques employed in preparing the surfaces and the methods used in characterizing the physical properties of the observed surfaces.

2.1 Polarimetric Scatterometer System

Two fully polarimetric truck-mounted scatterometer systems operating at 35 GHz and 94 GHz were used to conduct the experiments reported in this paper. A block diagram of the overall system, as well as the RF front-end circuitry of the 35 GHz radar, are shown in Fig. 1.

The scatterometers are capable of measuring directly the Mueller matrix of a distributed target using the coherent-on-receive (COR) technique, [4]. With the COR technique, 4 to 6 different polarizations (V, H, 45L, LHC, 135L, and RHC) are transmitted sequentially. Each radar is capable of simultaneous detection of the vertical and horizontal components of the backscattered signal, preserving the phase-difference between the two components. The Stokes vector of the scattered field is recorded for each transmitted polarization and then the Mueller matrix of the target is determined from the ensemble averages of the measured Stokes vectors, following the procedure outlined by Ulaby *et al.* [4,5].

The calibration of the scatterometers was performed in two steps. First, the receiver was calibrated using an odd-bounce reflector (a metallic sphere) and a polarizing grid placed infront of the receiving antenna. The receiver distortion matrix was determined by making the measurements with the polarizer positioned at each of three different angles. Second, the actually transmitted polarizations were determined using the calibrated receiver and the odd-bounce reflector. More details on the calibration technique are given in [6].

2.2 Surface Preparation and Characterization

The wavelengths corresponding to 35 and 94 GHz are 8.6 mm and 3.2 mm, respectively. To insure that the backscattering measurements cover a wide range of surface roughness relative to λ, special care was taken in preparing the three soil surfaces. Initially, all the surfaces were cleared from grass and vegetation debris. Then, in order to have a "smooth" surface with rms height less than 1 mm, a heavy roller was moved across surface S1. This technique resulted in a compacted soil medium with an rms height $s = 0.66$ mm. Surface S2 was a slightly rough surface with $s = 2.62$ mm, and for surface S3 the top layer was turned over by a farm implement resulting in an undulating surface with $s = 7.77$ mm. Surface height characterization was performed by a laser profiler, as discussed later. A summary of the roughness parameters for the three surfaces is given in Table 1. Two sets of measurements

were conducted, one for dry soil conditions and the other for wet soil conditions (see Table 2).

For each soil surface, the radar backscatter data was collected at incidence angles of 20^o, 45^o, and 70^o , under wet and dry soil conditions. For all observations, the distance from the radars to the surfaces was kept at about 10 m. Furthermore, to achieve good statistical representation of the measured backscatter, sixty independent spatial samples were collected for each surface. Additional independent samples were obtained by frequency averaging over the 1-GHz bandwidth. Data was collected *via* the network analyzer in raw-data format and then stored on the computer hard disk. The raw data was then postprocessed to separate the unwanted short-range returns from the target return using the time-domain gating capability of the system. Once the gated data was calibrated, the Stokes vectors measured for each polarization were then averaged over the independent samples. Finally, the Mueller matrix of the distributed target was determined.

Although both the backscattering coefficients, σ^o_{vv}, σ^o_{hh}, and σ^o_{hv}, and the statistics of the phase-differences, ϕ_{hh-vv} and ϕ_{hv-vv}, can easily be derived from the Mueller matrix [7], only the backscattering coefficients are discussed in this paper. The measured phase-difference statistics are the subject of a separate report.

The height profile of each soil surface was measured by a laser profiler mounted on an x-y table. The profiler, which is driven by stepper motors, measured 30-cm long linear segments with 0.3 mm horizontal resolution and 0.1 mm vertical resolution. An IBM-PC computer was used to control the stepper motors and to collect and store the heights measured by the laser profiler. At least five height profiles of different areas were recorded for each surface. The rms height s and correlation length l are listed in Table 1 for each of the three surfaces. More details on the measured surface height profiles are given in Appendix A.

The soil particle size distribution is shown in Fig. 2, indicating that the bulk of the soil material consist of fine sand. To investigate the void size distribution of the soil medium, thin

soil slices were collected and then photographed by a microscope camera. Two histograms of the void-size distribution were generated, one for bulk soil density $\rho_b = 1.69\ g/cm^3$ (Fig. 3(a)) and the other for $\rho_b = 1.32\ g/cm^3$ (Fig. 3(b)), by treating the voids as spherical in shape. It is worth noting that the mean void diameter is 0.165 mm for the high-density soil, compared to 0.242 mm for the low-density soil.

In conjunction with the radar measurements, the soil bulk density ρ_b and the volumetric moisture content m_v were measured by collecting 1-cm thick soil samples for each of the top 3 cm soil layers. The average values of ρ_b and m_v are listed in Table 2, for all three surfaces.

In order to compare the radar observations to theoretical models, we need to obtain good estimates of the soil's dielectric constant or relate the dielectric constant to the soil's physical properties. Unfortunately, no theoretical or empirical model is available in the literature that can correctly predict the effective dielectric constant of soils at MMW frequencies. In this paper, the effective dielectric constant of the soils observed in this study will be estimated by applying the semi-empirical formula found in [8,9]. The results are given in Table 2. For the measured dry surfaces with low moisture content, it is difficult to determine accurately the amount of free water. In addition, it was observed that the first few millimeters of the soil medium were very dry, and the soil wetness increased gradually with depth. Since the soil medium has a shallow penetration depth at MMW frequencies, we have chosen to set $m_v = 0.0$ for the dry surfaces, and to use that in the empirical formula (found in [8,9]) to determine the effective dielectric constants of those surfaces.

3 SURFACE SCATTERING

This section examines the experimental behavior of the backscattering coefficient σ^o as a function of (1) the radar parameters: frequency, receive-transmit polarization configuration, and the incidence angle θ, and (2) the soil surface parameters: the rms surface height s,

and moisture content m_v. Where appropriate, semi-empirical expressions are introduced to characterize the observed radar response. This is done in lieu of using theoretical models because comparison of the measured data with values calculated in accordance with the commonly available scattering models (small perturbation, physical optics, and geometric optics) reveals poor agreement between the theoretical predictions and the experimental observations. For more details on the results of this comparison, the reader is referred to Appendix B.

In general, two scattering mechanisms, shown in Fig. 4, contribute to the backscattering coefficient σ^o, a surface scattering contribution σ^s which is a function of the surface height statistics and ϵ_r of the lower half space, and a volume scattering contribution σ^v that is due to inclusions underneath the rough interface:

$$\sigma^o_{ij} = \sigma^s_{ij} + \sigma^v_{ij} \qquad\qquad i,j = h \text{ or } v. \tag{1}$$

The volume scattering contribution is in turn governed by the height statistics of the rough interface and the size and shape distributions of the inclusions in the soil medium (which are the voids in our case) and the dielectric constant of the host materials (soil particles). Calculations based on radiative transfer theory reveal that σ^v is much smaller than the observed scattering coefficient σ^o, and hence much smaller than σ^s, except for dry soil at 94 GHz. This can be explained by noting that at 35 GHZ the air voids are very small in size (see Fig. 3) relative to λ, and at 94 GHz the attenuation in wet soil reduces the penetration depth to a very thin surface layer, thereby reducing the volume scattering contribution to a negligable level. First, we will limit the analysis to the wet soil cases in order to examine the surface scattering component alone and then we will use radiative transfer theory to model the volume-scattering component (Section 4). Hence, for the cases presented in this section, $\sigma^o = \sigma^s$.

As was stated earlier, the radar observations were made at 35 GHz and 94 GHz for each

of three surfaces with widely different roughnesses. Figure 5 displays the angular variation of σ^o, for each of the three principal polarization configurations, for the surface with the smallest value of ks (surface S1 with $s = 0.66$ mm, observed at 35 GHz) and the surface with the largest value of ks (surface S3 with $s = 7.77$ mm, observed at 94 GHz). We note that the curves for the co-polarized scattering coefficients, σ^o_{vv} and σ^o_{hh}, diverge as a function of θ for the smooth surface represented by Fig. 5(a), but they remain approximately equal for the very rough surface represented by Fig. 5(b). This behavior is consistant with previous observations made at centimeter wavelengths [1]. We also note that the difference in level between the σ^o_{vv} and σ^o_{hv} curves is at least 18 dB for the smooth surface (actually 21 dB at 20°, decreasing to 18 dB at 70°), whereas the difference never exceeds 13 dB for the very rough surface. These observations clearly indicate that surface roughness exercises a significant influence on both the co-polarized ratio $p = \sigma^s_{hh}/\sigma^s_{vv}$ and the cross-polarized ratio $q = \sigma^s_{hv}/\sigma^s_{vv}$. It should be noted that the continuous curves shown in Fig. 5 are based on the semi-empirical expressions introduced later in this section.

3.1 Co-Polarization Ratio

The dependences of the ratios p and q on ks are illustrated further in Fig. 6. At $\theta = 20°$, p exhibits no discernible dependence on ks, as expected, because θ is close to normal incidence. At the higher angles of 45° and 70°, p increases with increasing ks until ks reaches a value of 4, beyond which p assumes the constant ratio of 1.0. The continuous curves shown in Fig. 6(a) are based on the following expression:

$$p = \frac{\sigma^s_{hh}}{\sigma^s_{vv}} = \left[1 - \left(\frac{2\theta}{\pi}\right)^{1/(3\Gamma_o)} exp[-0.4ks]\right]^2 \tag{2}$$

where θ is the incidence angle in radians and Γ_o is the reflectivity for normal incidence,

$$\Gamma_o = \left|\frac{1-\sqrt{\epsilon_r}}{1+\sqrt{\epsilon_r}}\right|^2 \tag{3}$$

The form of (2), which was adapted from the experience gained previously from the centimeter-wave study [1], includes a dependence on the dielectric constant ϵ_r. The plot shown in Fig. 5(a) corresponds to $\epsilon_r = 5.07 + j2.56$, which is in the middle of the range of the dielectric constants corresponding to the wet-soil surfaces observed by the radar (see Table 2). Thus, part of the data scatter in Fig. 6(a) is attributed to the non-uniformity of dielectric constants among the data points.

3.2 Cross-Polarization Ratio

The cross-polarization ratio q, which exhibits an inverse negative exponential dependence on ks for all angles of incidence (Fig. 6(b)), is modeled by the expression:

$$q = \frac{\sigma^s_{hv}}{\sigma^s_{vv}} = 0.23\sqrt{\Gamma_o}\,[1 - exp(-0.5\,sin\theta\,ks)] \tag{4}$$

To eliminate the dependence on the dielectric constant ϵ_r, the ratio q shown in Fig. 6(b) has been normalized by dividing it by $\Gamma_o^{1/2}$ for both the data points and the expression given by (4).

3.3 σ^s_{vv} Response

So far we have characterized the ratios of σ^s_{hh} and σ^s_{hv} with respect to σ^s_{vv} through (2) and (4). Now, we turn our attention to the response of σ^s_{vv} to θ, ks and ϵ_r. The proposed functional form is:

$$\sigma^s_{vv} = g\,\frac{cos^x\theta}{\sqrt{p}}\,[\Gamma_v(\theta) + \Gamma_h(\theta)] \tag{5}$$

where p is given by (2), $\Gamma_v(\theta)$ and $\Gamma_h(\theta)$ are the Fresnel reflectivities at incidence angle θ for v and h polarizations, respectively, and the function g is given by:

$$g = 2.2\,(1 - exp[-0.2ks]) \tag{6}$$

The exponent of the $\cos\theta$ term in (5) accounts for the change in the angular dependency

of σ^s_{vv} as a function of ks, and is given by:

$$x = 3.5 + \frac{1}{\pi}\, tan^{-1}[10\ (1.65 - ks)] \tag{7}$$

For a very rough surface with ks very large, $p \approx 1$, $g \approx 2.2$, and $x \approx 3$, in which case (5) reduces to:

$$\sigma^s_{vv} = 2.2\ \cos^3\theta\ [\Gamma_v(\theta) + \Gamma_h(\theta)]\ , \qquad for\ ks >> 1 \tag{8}$$

The inclusion of the sum $[\Gamma_v(\theta) + \Gamma_h(\theta)]$ in the expression for σ^s_{vv} simply insures that for a very rough surface, $\sigma^s_{vv} = \sigma^s_{hh}$ and yet the magnitudes of these two co-polarized coefficients are somehow related to the angle-dependent reflectivity of the surface.

To compare the proposed model with the experimental data (Fig. 7) we first normalized the measured values of σ^s_{vv} by dividing each by the sum of the reflectivities corresponding to the dielectric values associated with the surface and incidence angle and then plotted the results as a function of ks. The same normalization procedure was applied to (5) prior to plotting it in Fig. 7. In fact, the values of the coefficients appearing in (6) and (7) were selected by matching the expression given by (5) to the data.

3.4 Comparison of Model with Observations

The expressions given by (2)-(7) represent a semi-empirical model for characterizing the surface-scattering component of millimeter-wave backscattering from a random rough surface. The continuous curves shown in Fig. 5 are based on this model as are the curves shown in Fig. 8 for surface S2 (with intermediate roughness) and in Fig. 9 where the model is compared with the data reported by Yamasaki, *et al.* [3] at 60 GHz, also for wet-soil surfaces.

4 VOLUME SCATTERING

Before we embark on a detailed examination of σ^v, the volume backscattering contribution to the total backscattering coefficient σ^o, it would be instructive to examine the evidence we have in support of conducting such an examination in the first place. After all, studies conducted at centimeter wavelengths have shown that the behavior of the backscatter from random surfaces can be explained by surface scattering alone, without the need to add a volume-scattering contribution. The need to consider volume scattering at millimeter wavelengths can be illustrated through an examination of the experimental data shown in Fig. 10 which include a set of plots of σ^o_{hh} and σ^o_{hv} for a dry soil surface and another set for the same surface immediately after wetting the surface with a fine mist using a sprinkler system, thereby preserving the roughness of the surface. According to surface scattering models, both theoretical and empirical, increasing the soil moisture content causes the level of σ^o to increase at all angles of incidence for all polarization configurations. This is not the type of behavior observed in Fig. 10. For HH polarization, σ^o_{hh} of the dry surface is slightly lower than that for the wet surface at $\theta = 20^o$, but σ^o_{hh} for the dry soil is *higher* than that for the wet surface at 70^o. A similar, but even more pronounced, behavior is observed for HV polarization. The explanation for these observations stems from the following properties:

1. Surface scattering increases with increasing moisture content (dielectric constant), as stated earlier.

2. For surface scattering, σ^s varies with θ as $\cos^3\theta$ to $\cos^4\theta$, depending on surface roughness.

3. Volume scattering decreases with increasing moisture content, in part because the air-soil transmission coefficient decreases with increasing moisture content and in large part because the extinction in the soil medium increases rapidly with moisture content.

4. The volume scattering coefficients exhibit a very weak response as a function of the incidence angle θ.

5. The dimensions of the air voids (see Fig. 3) which constitute the scattering particles in the soil medium, are such that the scattering is in the Rayleigh region, which exhibits a λ^{-4}–dependence. Consequently, volume scattering is insignificantly small at centimeter wavelengths, but becomes important at millimeter wavelengths when the soil surface is dry.

4.1 Radiative Transfer Theory

To compute the volume-scattering contribution, we propose to use radiative transfer (RT) theory. Since we've observed that moisture content increased gradually with depth and that wet soil was encountered around 3 cm beneath the surface, the soil medium is modeled here as a 3-cm thick dry soil layer comprised of air voids embedded in the soil background, overlying a wet soil half space as shown in Fig. 11. At every point on the surface, the boundary of the thin layer is approximated by an infinitely extended flat plane perpendicular to the local surface normal. Volume scattering in the thin layer is computed by solving the radiative transfer equation numerically with the local incidence angle determined from $(\hat{k}_i.\hat{n})$ where $\hat{k}_i$ is the unit vector denoting the direction of propagation of the incident wave. The total volume scattering is the incoherent addition of the volume scattering contributions emerging from all points on the surface, each weighted by the probability of occurance of its surface normal. This approach is similar to that reported in [8] for computing surface scattering from tilted perturbed planes. The details are given in Appendix C.

4.2 Results

Solution of the radiative transfer equations requires knowledge of the void's shapes, sizes, volume fraction and relative dielectric constant, in addition to the relative dielectric constants

of both the background solid soil material and the wet soil half space. In this paper, we have assumed that the air voids are spherical in shape with a relative dielectric constant $\epsilon_a = 1.0+j0.0$. The void-size distribution function shown in Fig. 3(a) was used in the solution of the RT equations for surfaces S1 and S2 while the size distribution function shown in Fig. 3(b) was used for surface S3. The relative dielectric constant of the background solid soil material was taken as $\epsilon_{ss} = 4.7$ based on the empirical formula $\epsilon_{ss} = (1.01+0.44\,\rho_{ss})^2-0.062$ reported in [9], where $\rho_{ss} = 2.65\,g/cm^3$ is the measured solid soil density (which agrees well with ρ_{ss} of sandy soils [8,9]). The effective dielectric for the wet soil half space was assumed to be $\epsilon_2 = 7.0+j4.0$ at 35 GHz and $\epsilon_2 = 5.0+j2.5$ at 94 GHz. The voids volume fractions given in Table 2 were calculated on the basis of the measured bulk densities and solid soil density, $\nu_a = 1-\rho_b/\rho_{ss}$.

For the dry soil surfaces, the total backscattering coefficients σ^o_{ij} (i, j = v or h) were computed according to (1) by adding incoherently the volume scattering contribution σ^v_{ij}, computed using the RT technique, to the surface scattering contribution σ^s_{ij}, calculated according to the empirical model described in the preceding section (equations (2)-(7)). Good overall agreement is observed between the computed values of σ^o_{ij} and the measured radar responses for all surfaces at both frequencies, as can be seen in Figures 12 through 14.

It must be pointed out that at 35 GHz, σ^o_{ij} is dominated by surface scattering with minimal contribution provided by volume scattering (σ^s_{ij} is typically larger that σ^v_{ij} by 10 dB). However, at 94 GHz the volume component is comparable to the surface component for the co-polarized scattering coefficients, as can be seen in Fig. 15(a), and for cross-polarization, σ^o_{hv} is dominated by the volume contribution (Fig. 15(b)).

5 CONCLUSIONS

The backscattering coefficients of three soil surfaces were measured as a function of incidence angle using two scatterometers operating at 35 GHz and 94 GHz. The soil surfaces, with roughnesses ranging between $ks = 0.48$ and $ks = 15.3$, were measured under wet and dry conditions. When compared to measurements, the PO and GO surface-scattering models, as well as the empirical surface-scattering model given in [1], failed to consistently predict the measured backscattering coefficients.

Analysis of the measured radar data indicates that in general both surface and volume scattering contributions are present at MMW frequencies. For wet soil conditions, surface scattering is the dominant contribution and it can be modeled using a set of semi-empirical expressions. The volume contribution is important when the soil surface is dry, particularly at 94 GHz. Using radiative transfer theory, the volume scattering contribution was calculated by treating the soil medium as comprised of air voids imbedded in a soil background. This approach, which led to good agreement with the experimental observations, indicates that at 94 GHz, for example, the surface and volume scattering components are of comparable magnitude for σ^o_{vv} and σ^o_{hh}, but for the cross-polarized σ^o_{hv}, volume scattering is the dominant contribution.

References

[1] Y. Oh, K. Sarabandi, and F.T. Ulaby, "An Empirical and an Inversion Technique for Radar Scattering from Bare Soil Surfaces," *IEEE Trans Geosci. Remote Sensing*, vol. GE-30, pp. 370-381, Mar. 1992.

[2] Y. Oh, K. Sarabandi, and F.T. Ulaby, "An Empirical Model for Phase Difference Statistics of Rough Surfaces," *Proceedings of IGARSS '93 Symposium*, Tokyo, Japan, vol. III, pp. 1003-1005, August 1993.

[3] H. Yamasaki, J. Awaka, A. Takahashi, K. Okamoto, and T. Ihara, "Measurements of Soil Backscatter with A 60 GHz Scatterometer," *IEEE Trans Geosci. Remote Sensing*, vol. GE-31, pp. 761-766, July 1992.

[4] F.T. Ulaby, M. Whitt and K. Sarabandi, "AVNA-Based Polarimetric Scatterometers," IEEE AP magazine, vol. 32, 1990.

[5] F.T. Ulaby and C. Elachi, *Radar Polarimetry for Geoscience Applications*, Artech House, 1990.

[6] J.B. Mead, "Polarimetric Measurements of Foliage and Terrain at 225 GHz," Ph.D. thesis, University of Massachusetts, Amherst, MA, 1990.

[7] K. Sarabandi, "Derivation of Phase Statistics of Distributed Targets from the Averaged Mueller Matrix," *Radio sci.*, vol. 27, pp. 553-560, Sept.-Oct. 1992.

[8] F.T. Ulaby, R.K. Moore, and A.K. Fung, *Microwave Remote Sensing*, Vol.II-III, Artech, 1986.

[9] M.C. Dobson, F.T. Ulaby, M. T. Hallikainen, and M.A. El-rayes, "Microwave Dielectric Behavior of Wet Soil-Part II: Dielectric Mixing Models," *IEEE Trans Geosci. Remote Sensing*, vol. GE-23, pp. 35-46, Jan. 1985.

[10] Y. Kuga, F.T. Ulaby, T.F. Haddock, and R. DeRoo, "Millimeter-wave radar scattering from snow: 1. Radiative transfer model," *Radio Sci.*, vol. 26, pp. 329-341, Mar.-April 1991.

surface	$s(mm)$	$l(mm)$	Freq(GHz)	ks	kl
S1	0.66	20	35	0.48	14.7
			94	1.3	39.4
S2	2.62	20	35	1.92	14.7
			94	5.16	39.4
S3	7.77	20	35	5.69	14.7
			94	15.3	39.4

s = rms height
l = correlation length
$k = 2\pi / \lambda$

Table 1: Surface roughness statistical parameters for the three soil surfaces.

			m_v		ϵ_r	
Surface	ρ_b	ν_a	0-1 cm	2-3 cm	35 GHz	94 GHz
S1-dry	1.69	0.36	0.02	0.08	(3.1, 0.05)	(3.1, 0.05)
S1-wet	1.69	0.36	0.23	0.19	(7.3,4.5)	(5.0,2.4)
S2-dry	1.37	0.45	0.04	0.07	(2.5, 0.05)	(2.5, 0.05)
S2-wet	1.37	0.45	0.12	0.12	(4.6,2.0)	(3.5,1.1)
S3-dry	1.32	0.50	0.04	0.07	(2.5, 0.05)	(2.5, 0.05)
S3-wet	1.32	0.50	0.19	0.18	(5.9,3.5)	(4.1,1.9)

ρ_b = soil bulk density (g/cm^3).
ν_a = air-voids volume fraction.
m_v = volumetric moisture content.
ϵ_r = effective dielectric constant.

Table 2: Summary of soil properties.

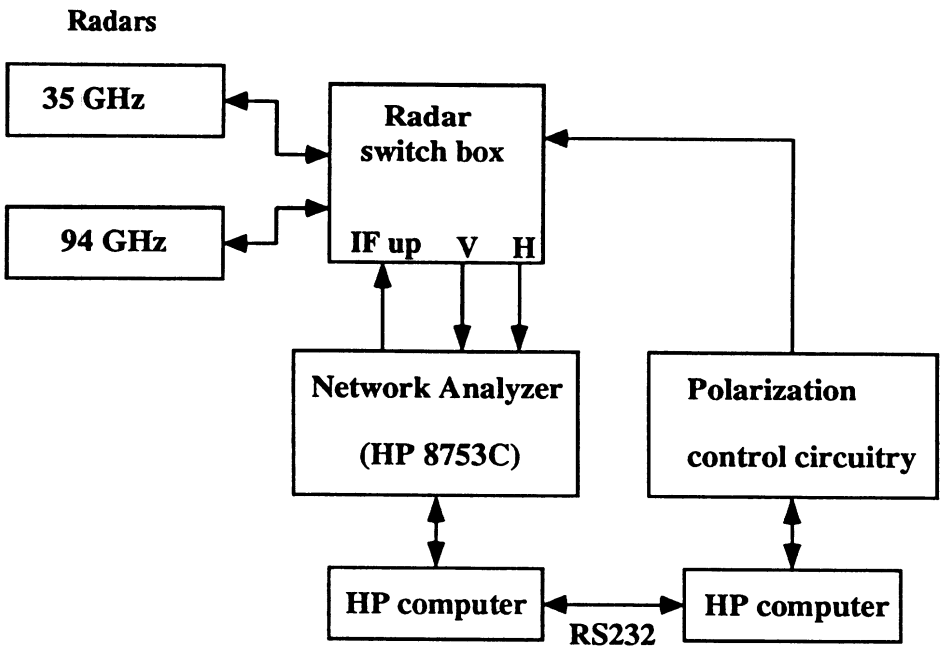

(a)

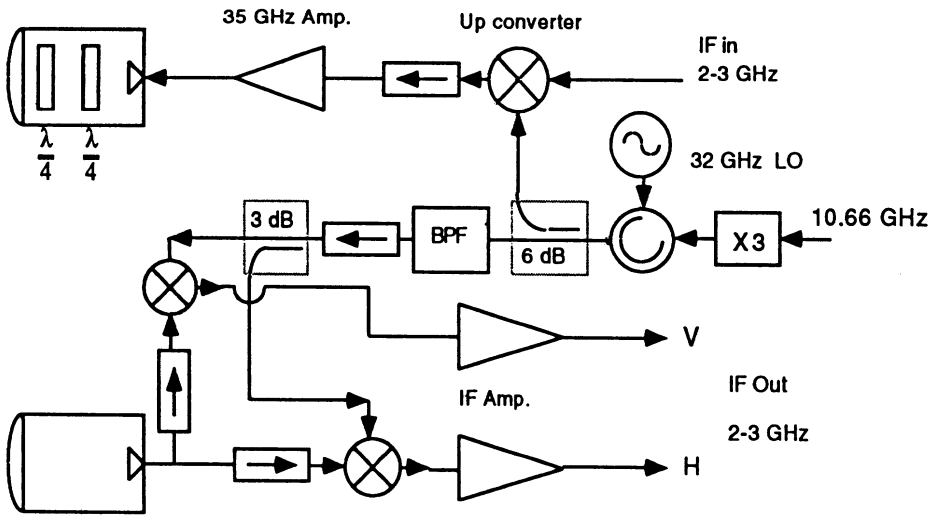

(b)

Figure 1: Overview diagram of the MMW polarimetric radar system (a) system block diagram, (b) RF front end circuitry of the 35 GHz radar.

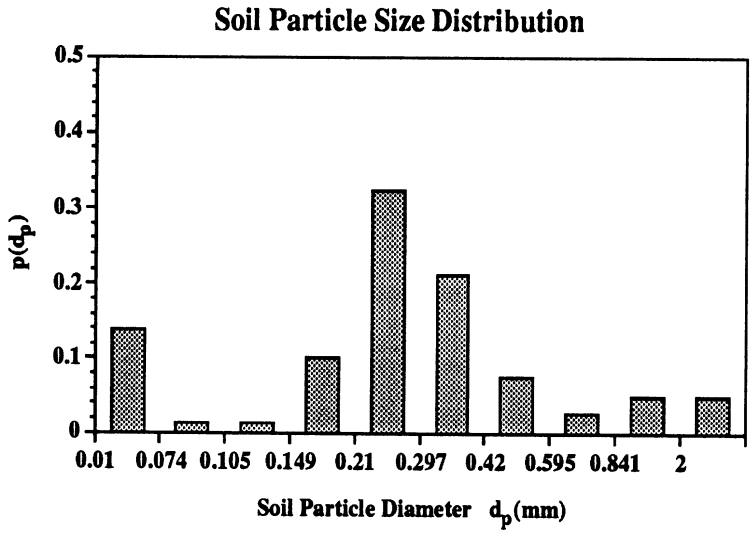

Figure 2: Soil particle size distribution $p(d_p)$.

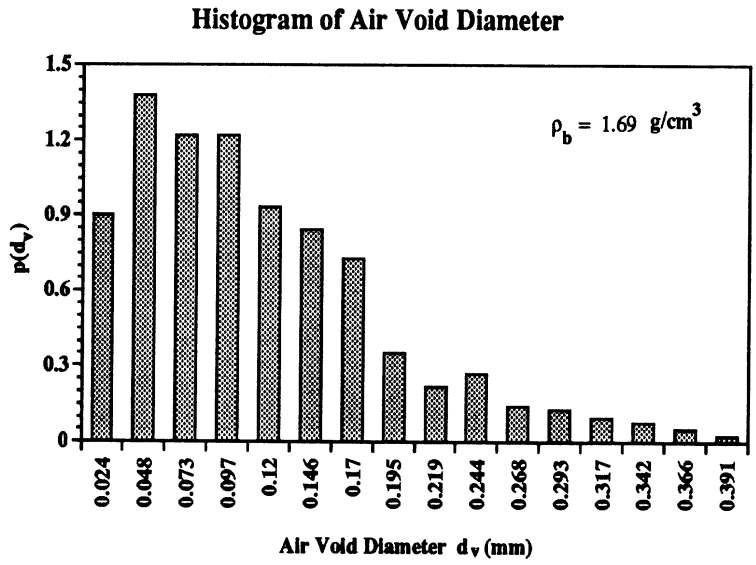

(a)

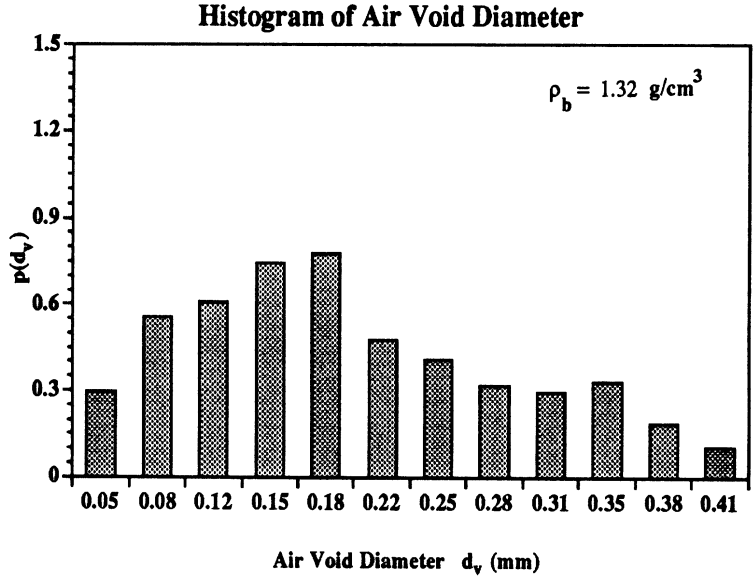

(b)

Figure 3: Histogram of the air voids diameter for soils with (a) $\rho_b = 1.69\, g/cm^3$, and (b) $\rho_b = 1.32\, g/cm^3$.

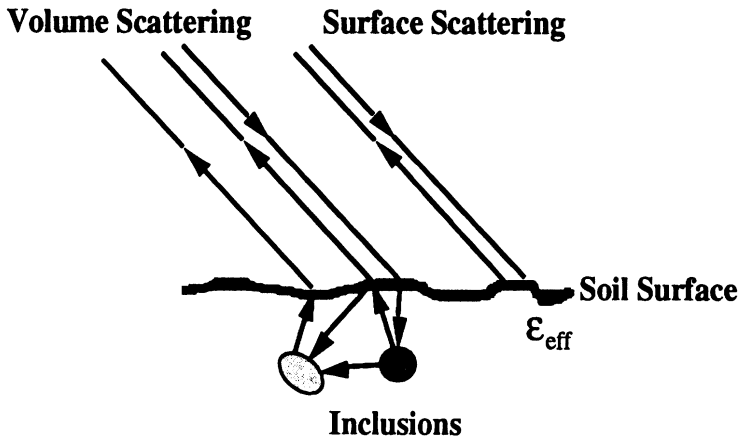

Figure 4: Surface and volume-scattering mechanisms contributing to the total backscatter.

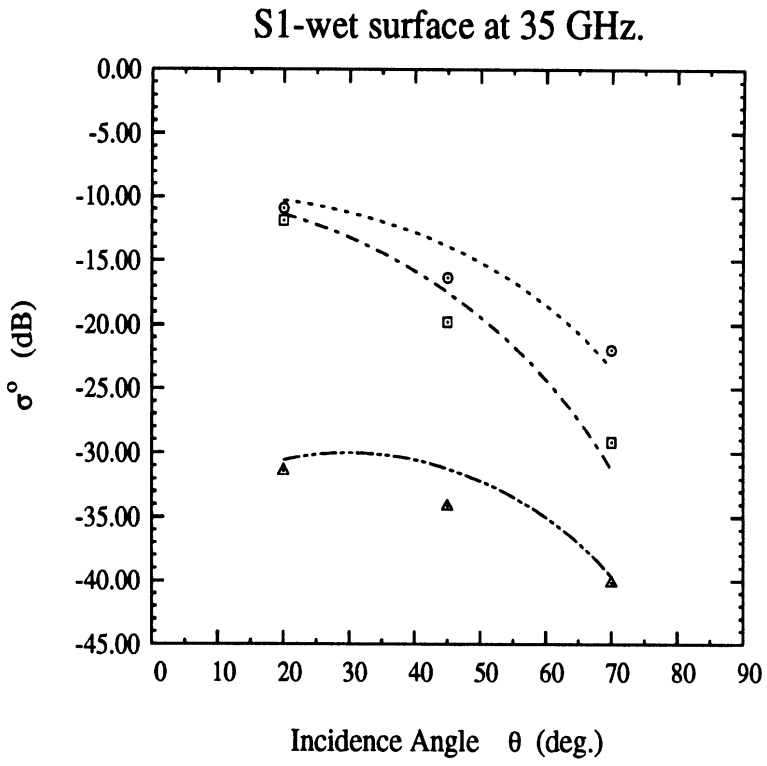

(a)

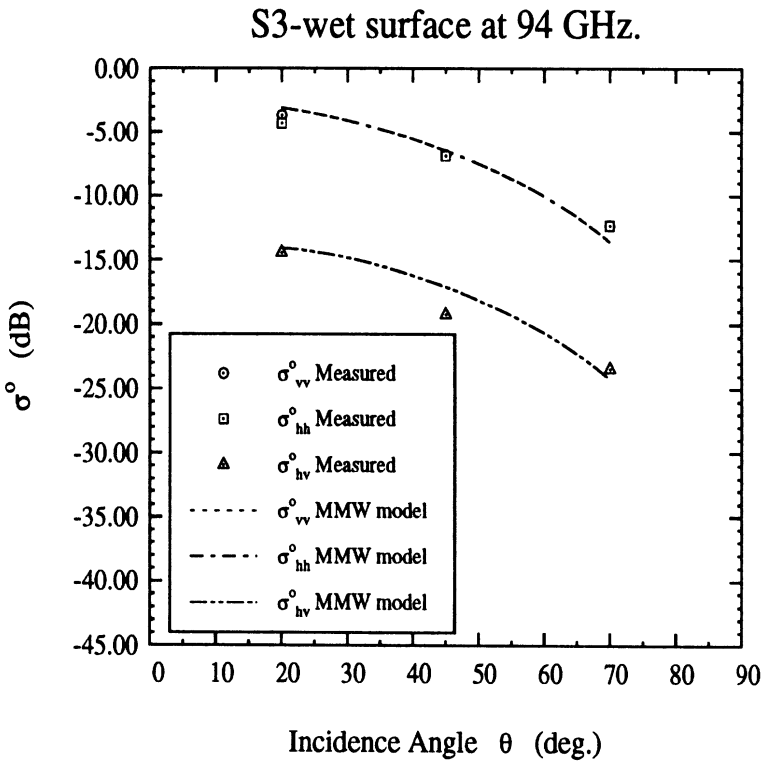

(b)

Figure 5: Comparison of the measured backscattering coefficients for wet soil surfaces with calculations based on the semi-empirical surface scattering model given in Section 3 for (a) the smoothest surface at 35 GHz ($ks = 0.48$), and (b) the roughest surface at 94 GHz ($ks = 15.3$).

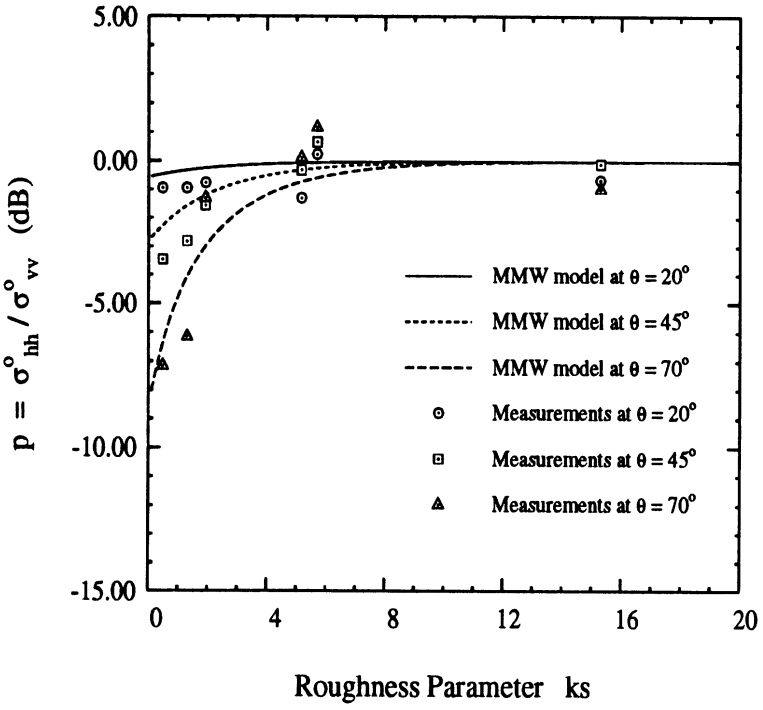

(a)

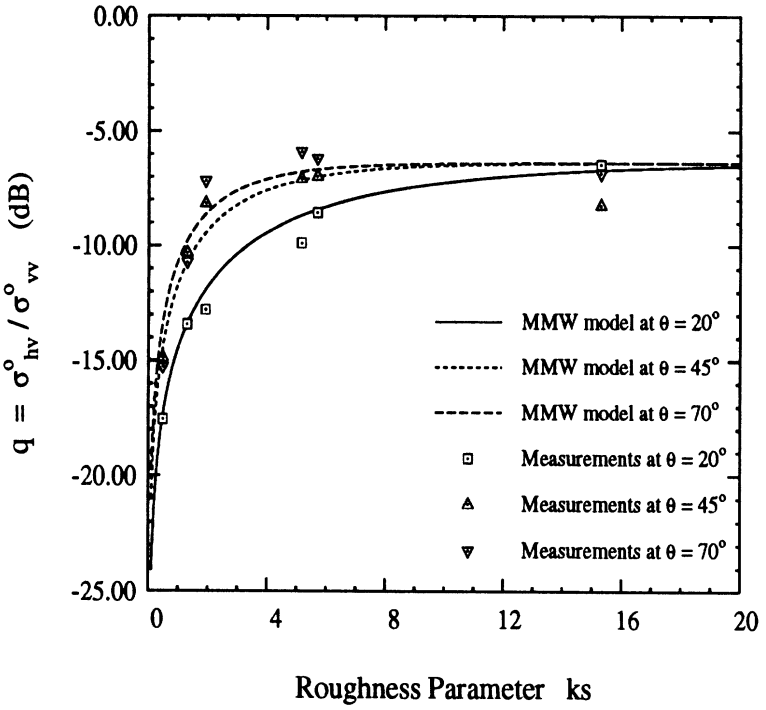

(b)

Figure 6: Measured sensitivity of (a) the co-polarized ratio p, and (b) the cross-polarized ratio q to surface roughness for wet soil surfaces at various incidence angles. The continuous curves are based on the expressions given in Section 3.

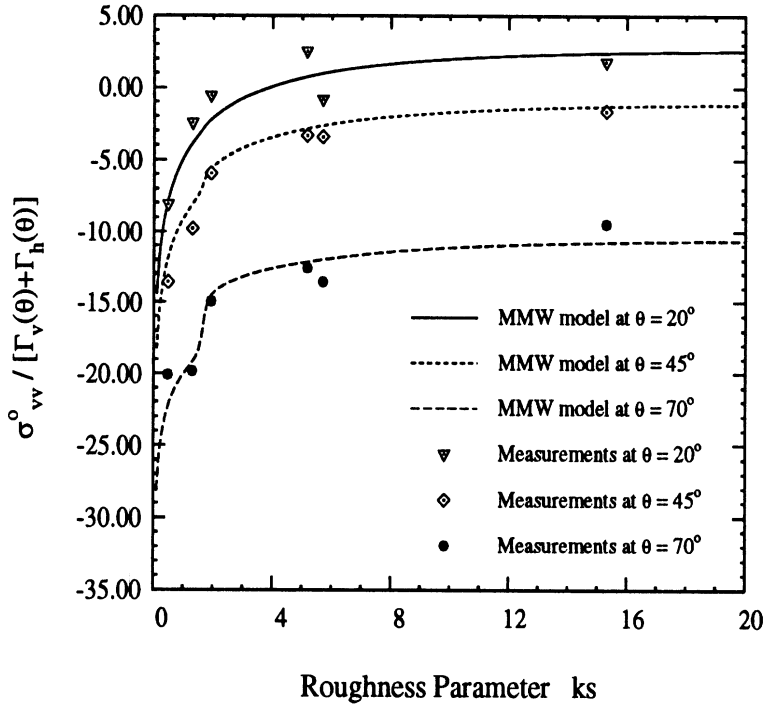

Figure 7: The sensitivity of σ^o_{vv} to surface roughness for wet soil at various incidence angles.

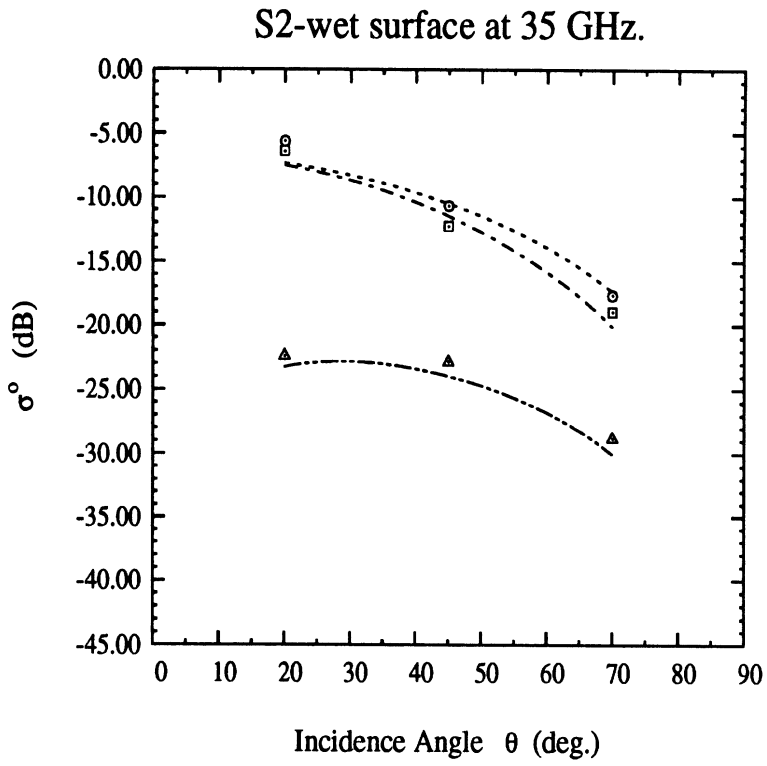

(a)

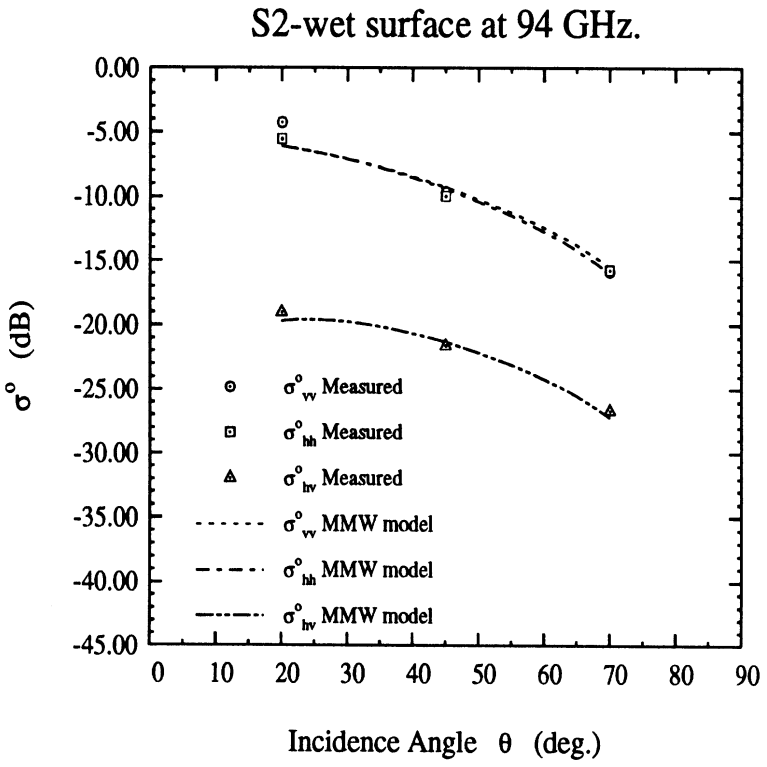

(b)

Figure 8: Comparison between measured data of S2-wet soil surface and the MMW semi-empirical surface scattering model at (a) 35 GHz, (b) 94 GHz.

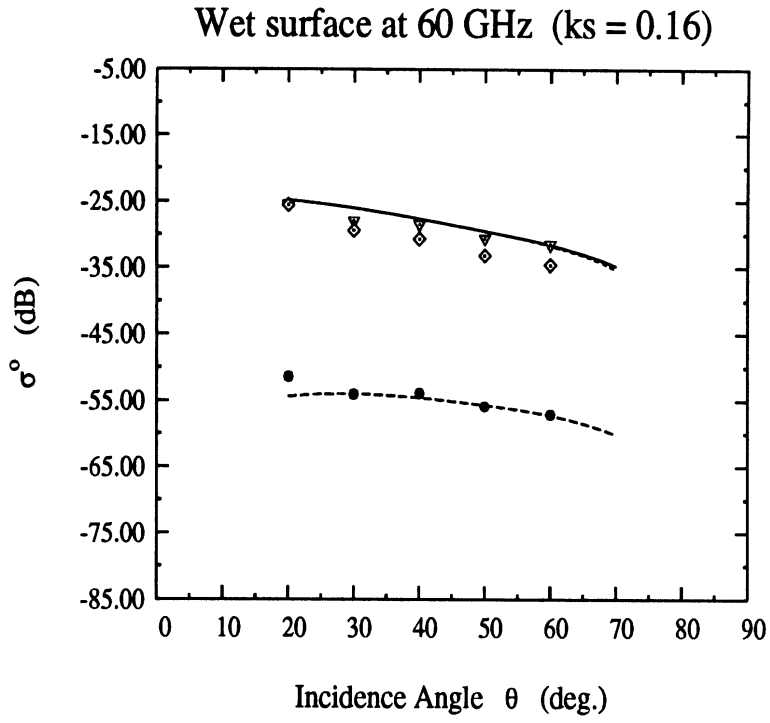

(a)

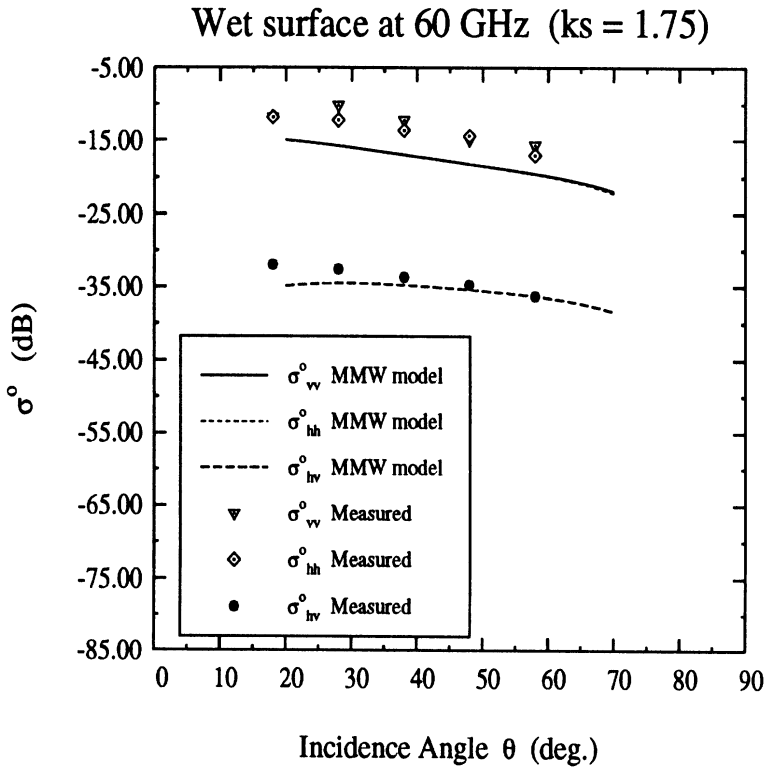

(b)

Figure 9: Comparison between measured data for wet soil surfaces ($\epsilon_r = 1.9 + j\,0.4$) at 60 GHz and the MMW semi-empirical surface scattering model for (a) $ks = 0.16$, and (b) $ks = 1.75$. (Data from Yamasaki *et al.* [3]).

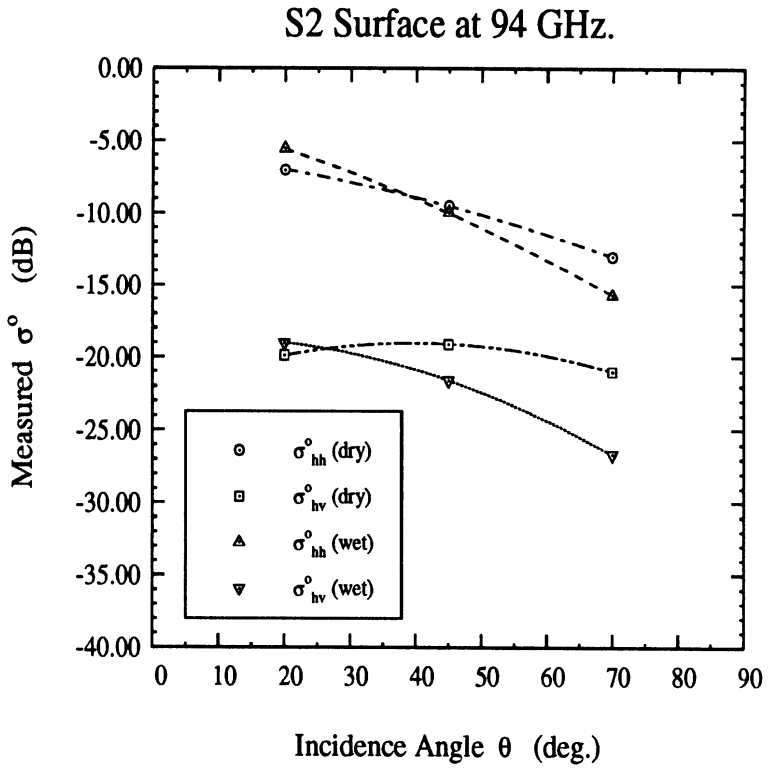

Figure 10: Measured σ^o_{hh} and σ^o_{hv} for wet and dry surface conditions at 94 GHz ($ks = 5.16$). Note that at 70°, σ^o(dry) is greater than σ^o(wet) for both polarizations, evidence of volume scattering contribution.

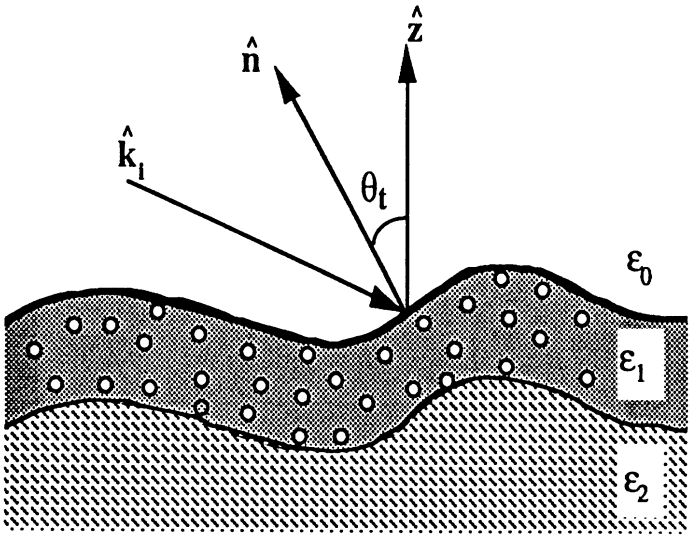

Figure 11: Proposed model for the dry soil medium.

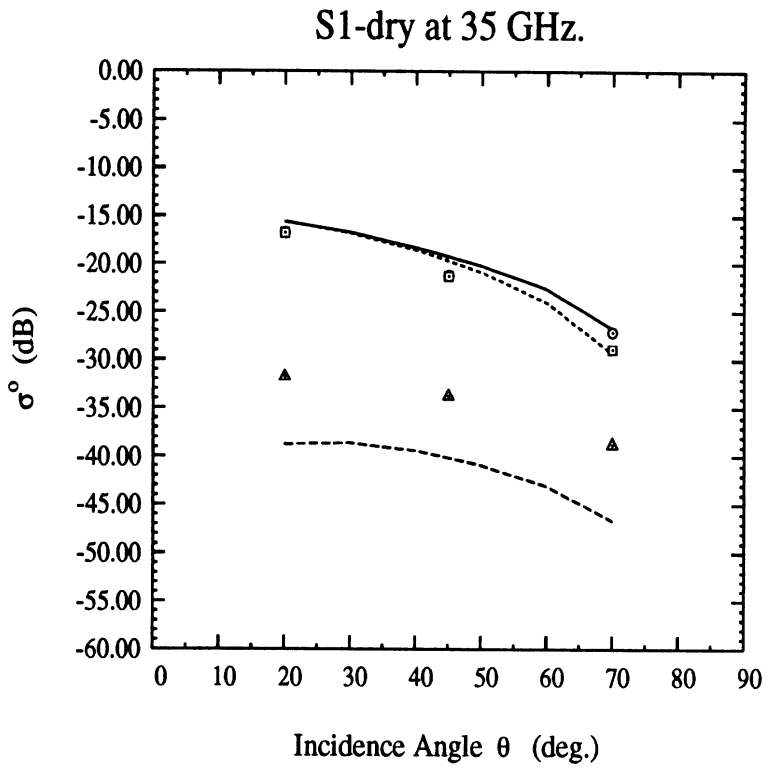

(a)

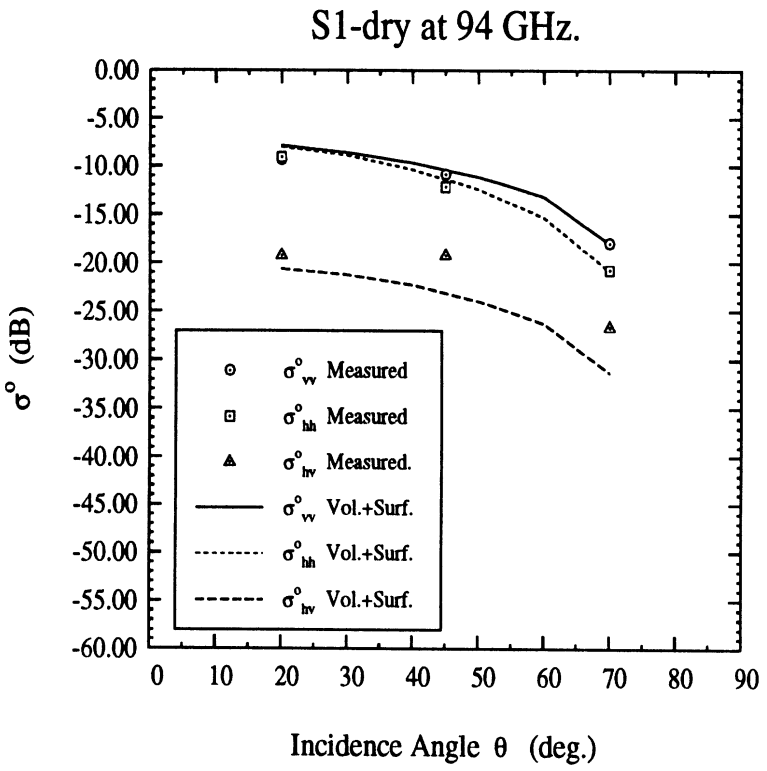

(b)

Figure 12: Comparison between the measured backscattering coefficient and the total backscattering coefficient σ^o predicted by the sum of surface and volume scattering contributions for surface S1 at (a) 35 GHz and (b) 94 GHz.

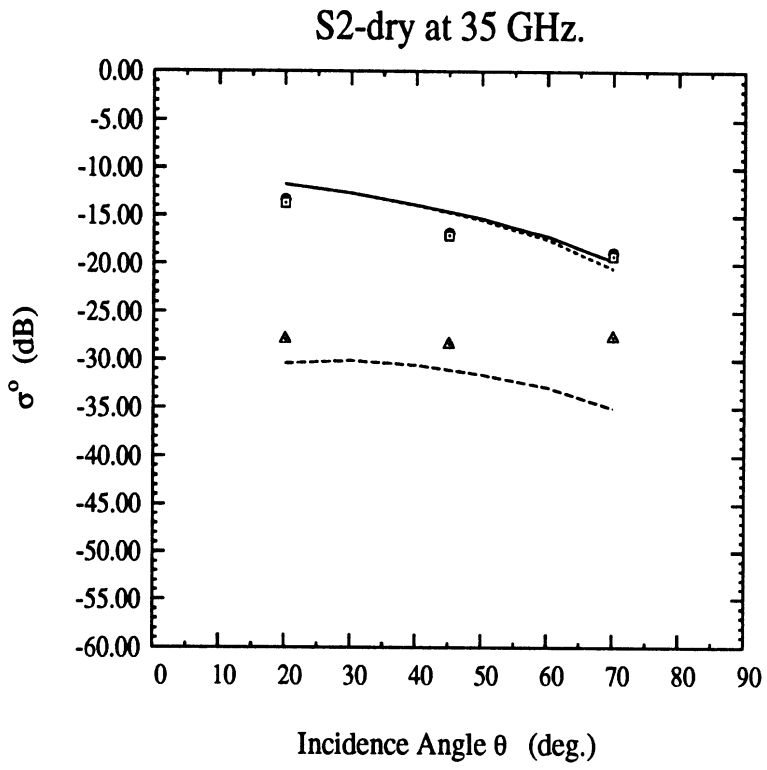

(a)

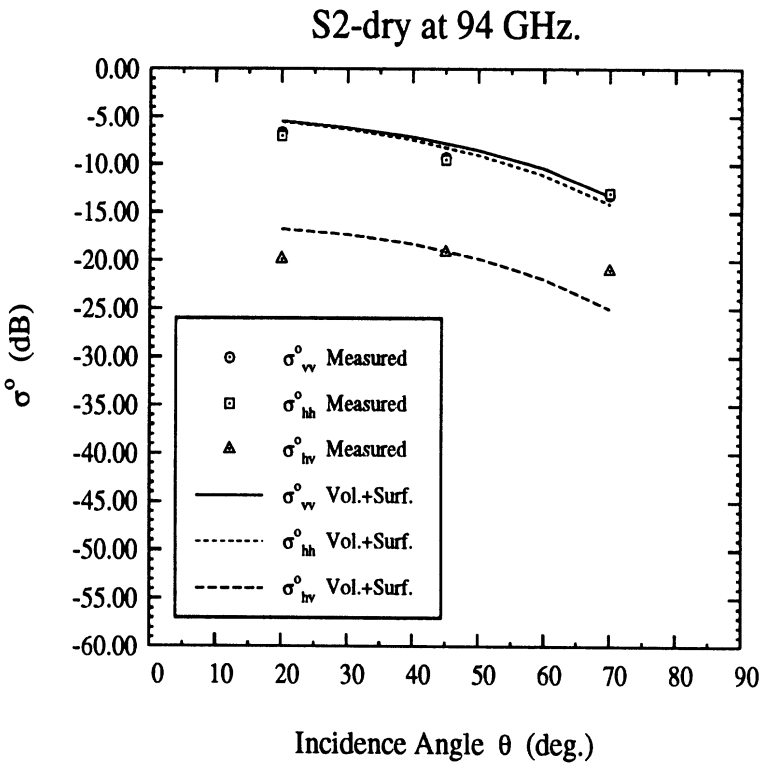

(b)

Figure 13: Comparison between the measured backscattering coefficient and the total backscattering coefficient σ^o predicted by the sum of surface and volume scattering contributions for surface S2 at (a) 35 GHz and (b) 94 GHz.

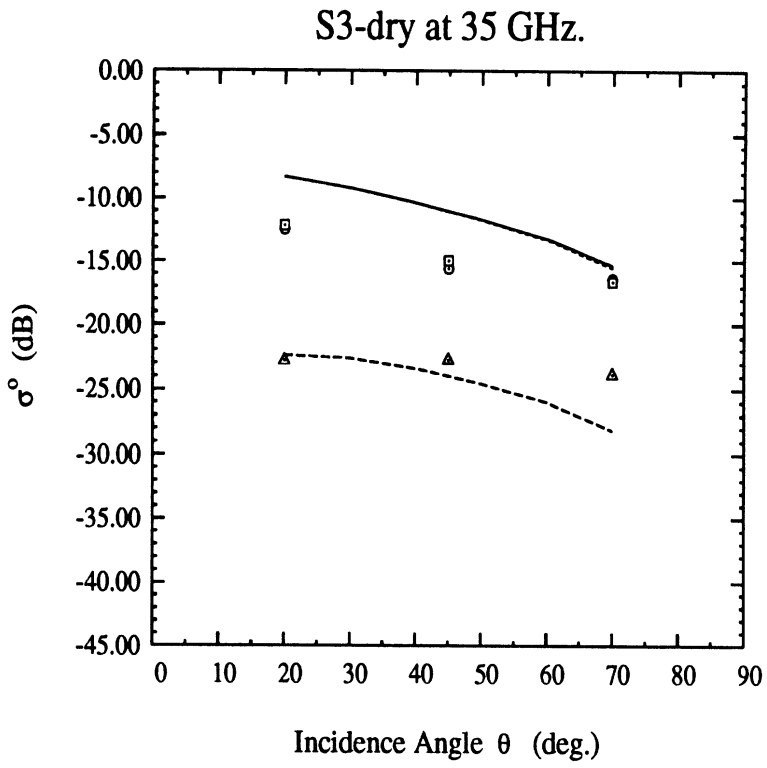

(a)

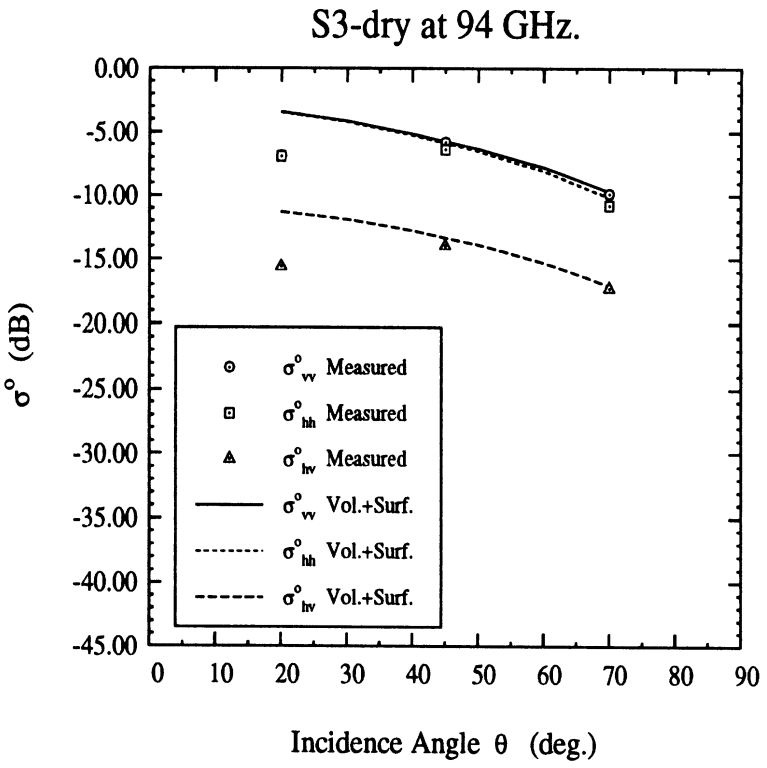

(b)

Figure 14: Comparison between the measured backscattering coefficient and the total backscattering coefficient σ^o predicted by the sum of surface and volume scattering contributions for surface S3 at (a) 35 GHz and (b) 94 GHz.

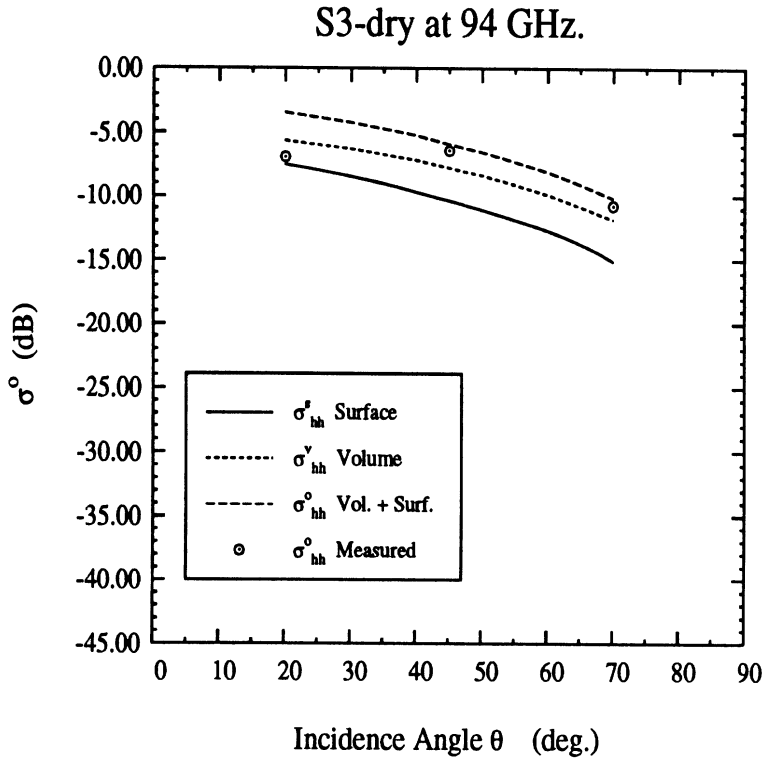

(a)

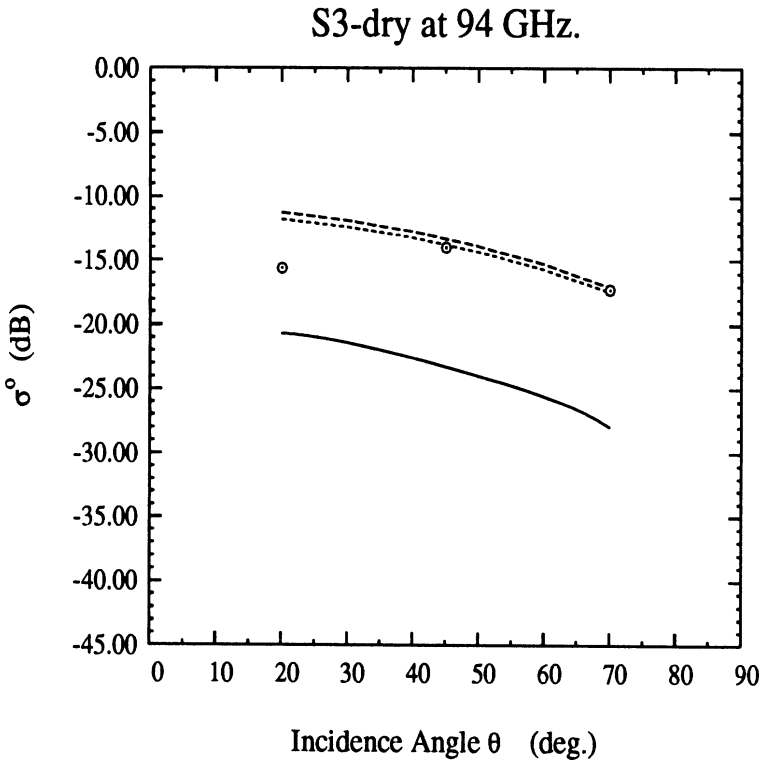

(b)

Figure 15: Comparison between the backscattering coefficients based on the surface-scattering component alone, the volume-scattering component alone, and the surface + volume scattering components added incoherently and the measured backscattering coefficients for (a) σ^o_{hh} (b) σ^o_{hv}.($ks = 15.3$).

APPENDIX A:

Preparation and Characterization of The Rough Soil Surfaces

Since the wavelengths corresponding to 35 GHz and 94 GHz (8.6 mm and 3.2 mm, respectively) are comparable to the dimensions of some of the soil particles, special care was taken in preparing the soil surfaces and characterizing both the height statistics of the air-soil interface and the soil medium contituents. Section A.1 describes the steps that were taken in preparing the soil surfaces while Section A.2 summarizes the soil surface statistics, the bulk soil densities, and the volumetric moisture contents of the three surfaces.

A.1 Surface Preparation

Initially, all surfaces were cleared from grass and vegetation debris since they are strong scatterers at MMW frequencies. Then, to insure that the backscattering measurements cover a wide range of surface roughness relative to λ, three surfaces were prepared as follows:

1. A heavy roller was moved across surface S1 in order to create a "smooth" surface with an rms height less than 1 mm. This technique resulted in a compacted soil medium with an rms height $s = 0.66$ mm.

2. No special preparation was performed on surface S2 which was a slightly rough surface with $s = 2.62$ mm.

3. The top layer of surface S3 was turned over by a farm implement resulting in a gently undulating surface with $s = 7.77$ mm.

The soil surfaces were sprayed with a fine mist of water droplets using a tree sprayer with an adjustable nozzle in order to maintain the volumetric moisture content constant

during the radar measurements of the wet soil surfaces while simultaneously preserving the surface roughness. Samples of the soil medium were collected frequently during the radar measurements of the soil surfaces to determine the moisture content. The gravimetric moisture content is summarized in Fig. A.1 for surfaces S1 and S3 as a function of time.

A.2 Surface Characterization

Surface height profiles and soil samples were collected for each soil surface under wet and dry conditions in order to determine the surface height statistics, the bulk soil density and the moisture content. In addition, size distributions of the solid soil particles and the air voids were generated (Fig. 2 & 3).

Surface Height

The height profile of each soil surface was measured by a laser profiler mounted on an x-y table. The profiler, which is driven by stepper motors, measured 30-cm long linear segments with 0.3 mm horizontal resolution and 0.1 mm vertical resolution. An IBM-PC was used to control the stepper motors and to collect and store the heights measured by the laser profiler. At least five height profiles of different areas were recorded for each surface. Figure A.2 shows samples of the surface height profiles collected for the three soil surfaces. In addition, Figure A.3 shows the corresponding auto-correlation functions of the surface profiles, each normalized to its maximam value at zero displacement. The rms height s and correlation length l are listed in Table 1 for each of the three surfaces.

Soil Density and Moisture Content

In conjuction with the radar measurements, the bulk soil density ρ_b and the volumetric moisture content m_v were measured by collecting 1-cm thick soil samples for each of the top 3 cm soil layers. The procedure is shown in Fig. A.4 where a 15 $\times$ 15 cm metallic frame of 1-cm thickness is placed on top of the soil surface and gently forced into the soil with minimal disturbance to the soil medium. The soil within the metallic frame is then removed

to a container and immediately weighed *via* a sensitive electronic scale, baked overnight in an oven and weighed once again when dry. The moisture content and the bulk doil density were determined using the following relations:

$$
\begin{aligned}
m_g &= \frac{W_{wet}}{W_{dry}} \\
\rho_b &= \frac{W_{dry}}{V} \\
m_v &= m_g \times V
\end{aligned}
$$

where W_{wet} is the weight of the soil before baking, W_{dry} is the weight of the soil after baking, m_g is the gravimetric moisture content, and V is the volume of the soil sample ($15 \times 15 \times 1\, cm^3$).

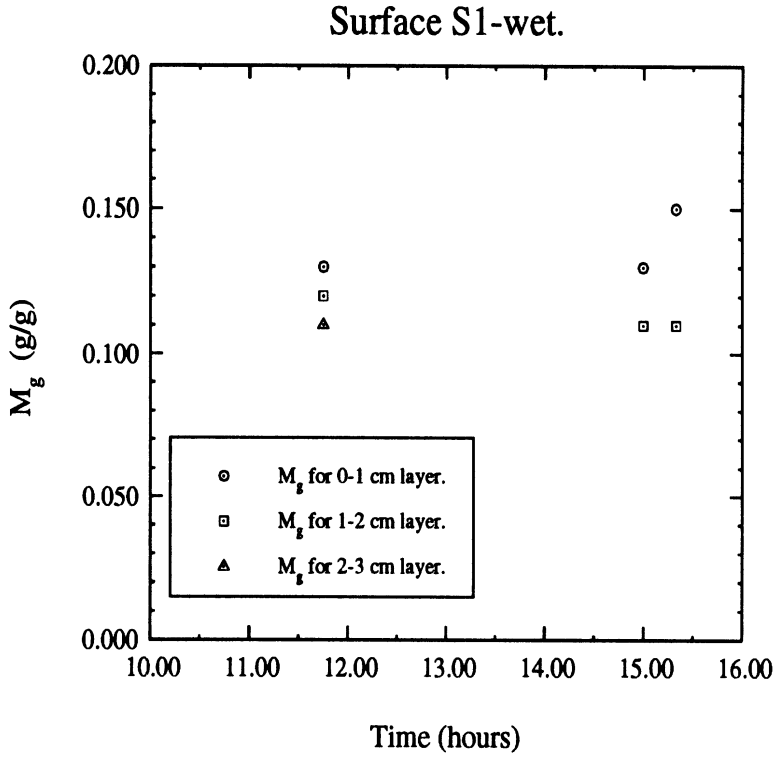

(a)

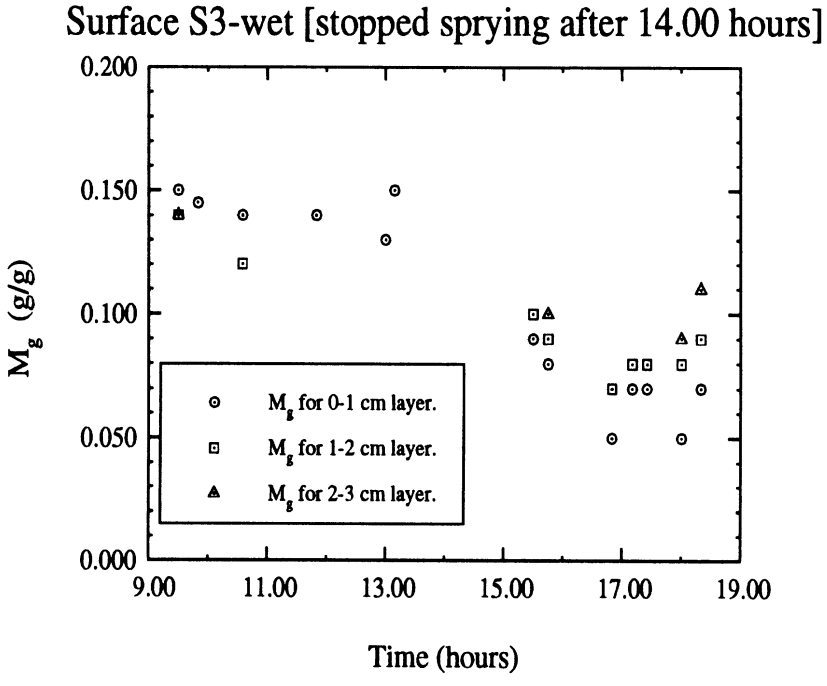

(b)

Figure A.1: The gravimetric moisture content m_g as a function of time for wet surfaces (a) S1, and (b) S3.

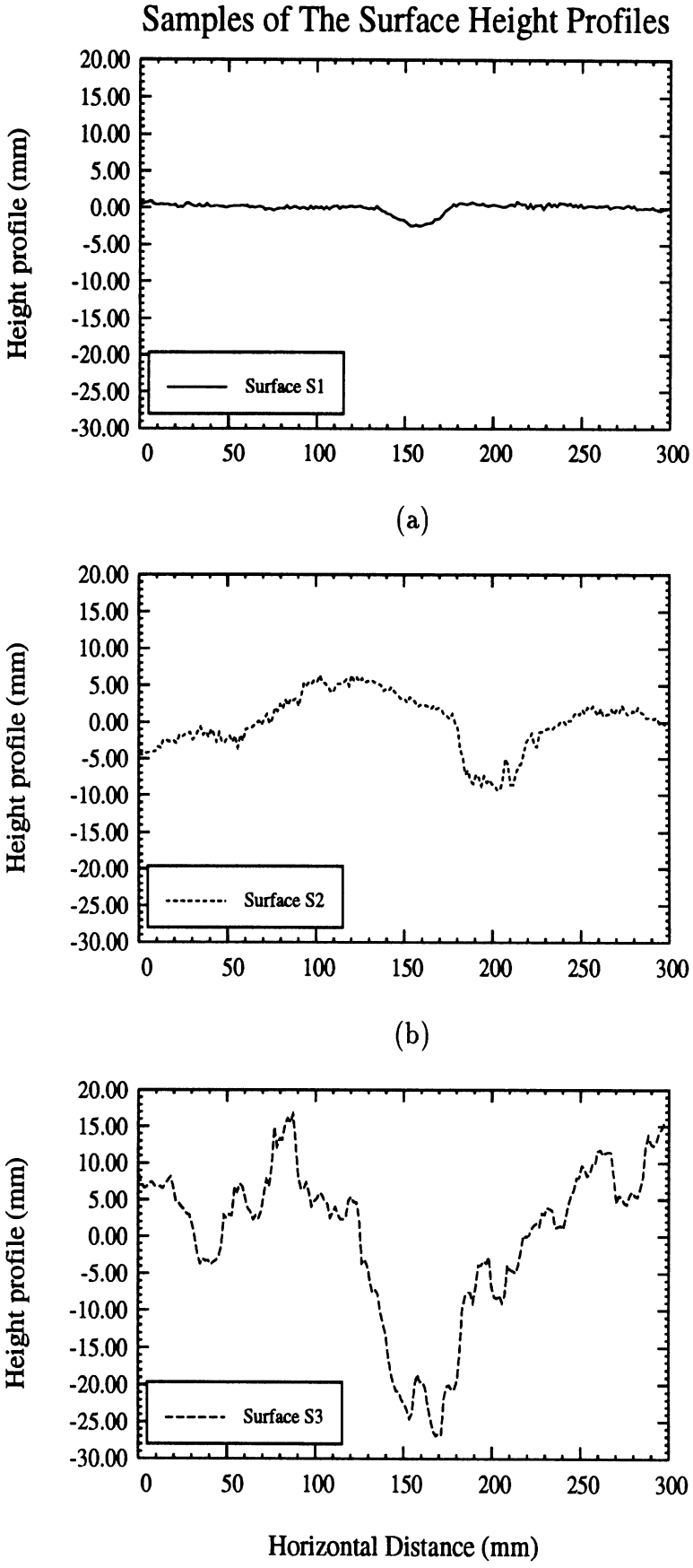

Figure A.2: Samples of the Surface height profiles, measured using a laser profiler, for surface (a) S1, (b) S2, and (c) S3.

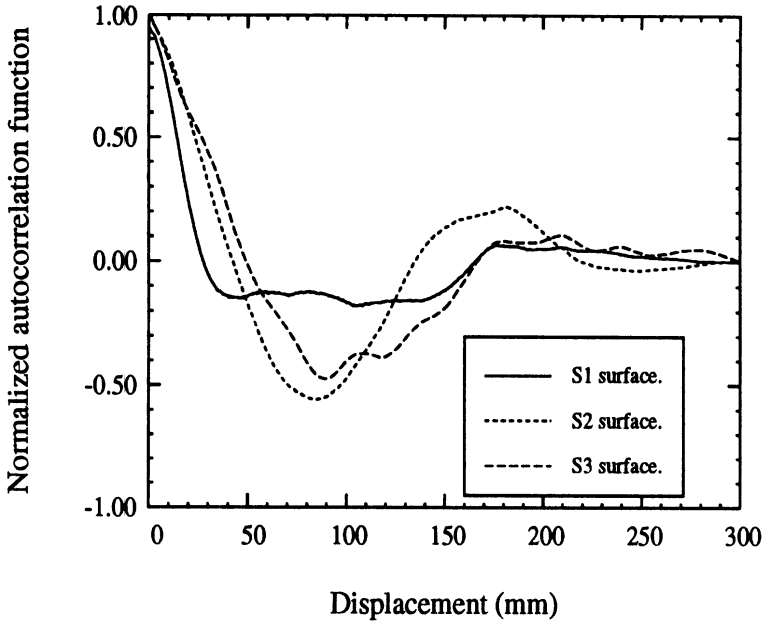

Figure A.3: Samples of the autocorrelation functions of the three surfaces.

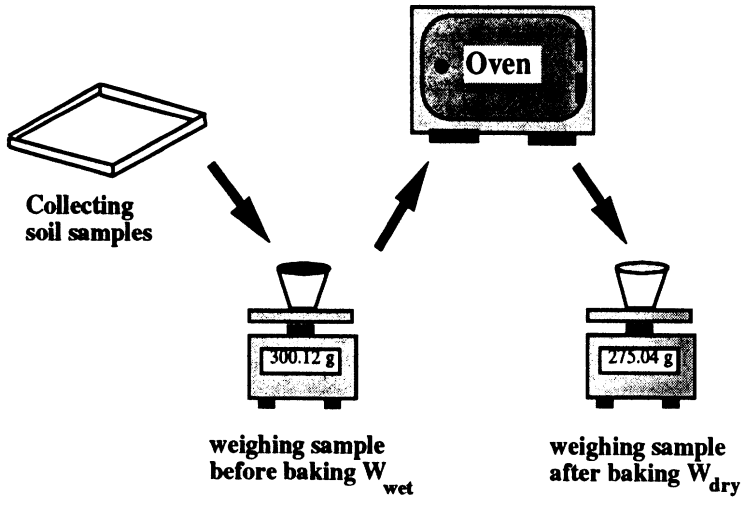

Figure A.4: The procedure used to measure the bulk soil density and the gravimetric moisture content.

APPENDIX B

Comparison Between Rough Surface Scattering Models and Measurements at Millimeter Wavelengths

In this appendix, the backscattering coefficients of the three soil surfaces measured at millimeter wavelengths as a function of incidence angle are compared to those predicted by theoretical models, namely the Physical Optics model (PO) and the Geometric Optics model (GO). Expressions for σ^o and the regions of validity of these models, for random rough surfaces with Gaussian auto-correlation functions, are given in [5,8]. It must be noted that none of the surfaces examined here fell within the regions of validity of the Small Perturbation model and hence no comparison with this model was conducted. In addition, the measured backscattering coefficients are compared to the coefficients predicted by the empirical surface scattering model [1] developed at L, C, and X microwave bands (henceforth, refered to in this paper as the LCX empirical model).

Both surfaces S1 and S2 and at both millimeter-wave frequencies are within the region of validity of the PO model. Being a single scattering model, the PO model cannot predict the cross-polarized return in the backscattering direction. Hence, only the co-polarized return is examined here. Upon comparing the measured σ^o to those computed *via* the PO model with the autocorrelation function assumed to be Gaussian (Fig. B.1), we observe that the PO model fails to predict the level of σ^o as well as its angular behavior. However, the values of σ^o, computed with an exponential autocorrelation function, matches the measured σ^o at the lower angles of incidence but underestimates it at the higher angles of incidence as shown in Fig. B.1. In addition, while our measurements indicate that $\sigma^o_{hh} \leq \sigma^o_{vv}$ for all surfaces and at both frequencies, consistant with the observations reported in [1] at microwave frequencies,

the PO model with the exponentail autocorrelation function predicts the opposite behavior.

Only surfaces S2 and S3 at 94 GHz and S2 at 35 GHz (for angles $\theta = 20^o, 45^o$) are within the regions of validity of the GO model. Similar to the PO model, the GO model does not predict any cross-polarized return in the backscatter direction. The measurements, on the other hand, show a significant cross-polarized return. The co-polarized backscattering coefficients computed using the GO model with a Gaussian autocorrelation function are compared to the measured data for surfaces S2 and S3 at 94 GHz in Fig. B.2.

The LCX empirical surface scattering model was based on measurements of σ^o_{vv}, σ^o_{hh} and σ^o_{hv} as function of the angle of incidence for four different surfaces at L, C, and X bands. The surface roughness and moisture content for the data used in developing the model covered the ranges: $0.1 < ks < 6.0$, $2.6 < kl < 19.7$ and $0.09 < m_v < 0.31$. In addition, data corresponding to $\theta = 30^o, 40^o, 50^o$ only was used in the development of the model. The empirical equations characterizing the model are summerized below for completeness

$$
\begin{aligned}
\sigma^o_{vv} &= g\,\frac{cos^3\theta}{\sqrt{p}}\,[\Gamma_v(\theta) + \Gamma_h(\theta)] \\
g &= 0.7\,\left[1 - exp(-0.65(ks)^{1.8}\right] \\
\sigma^o_{hh} &= p\,\sigma^o_{vv} \\
\sqrt{p} &= \sqrt{\frac{\sigma^o_{hh}}{\sigma^o_{vv}}} = 1 - [\frac{2\theta}{\pi}]^{1/(3\Gamma_o)}\ exp(-ks) \\
q &= \frac{\sigma^o_{hv}}{\sigma^o_{vv}} = 0.23\,\sqrt{\Gamma_o}\,[1 - exp(-ks)] \\
\Gamma_o &= \left|\frac{1-\sqrt{\epsilon_r}}{1+\sqrt{\epsilon_r}}\right|^2
\end{aligned}
$$

The LCX empirical model was tested against the surfaces reported in this paper. While only two surfaces are chosen here for detailed comparisons, the conclusions do apply to the third surface as well. The first surface is S1-wet at 35 GHz which has its ks, kl, and m_v

within the ranges covered by the LCX empirical model. For this surface, the LCX empirical model predicts σ^o_{vv} and σ^o_{hh} very well. However, it overestimates σ^o_{hv}, as shown in Fig. B.3. The second surface is S3-wet at 94 GHz which has its ks and kl outside the ranges covered by the LCX empirical model. For this surface, the model fails to predict the measured data for all polarizations, as shown in Fig. B.4.

The LCX empirical model does not predict the MMW backscattering response of soil surfaces in a consistent fashion.

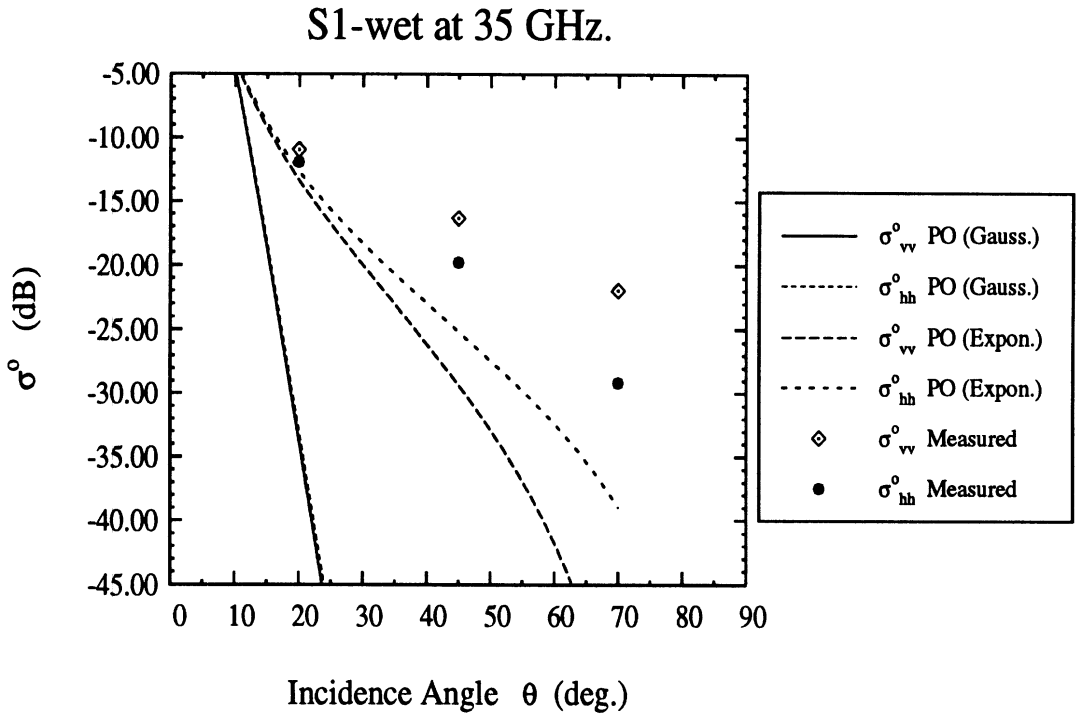

Figure B.1: Comparison between measured data and the PO model predictions at 35 GHz for gaussian and exponential surface height autocorrelation functions.

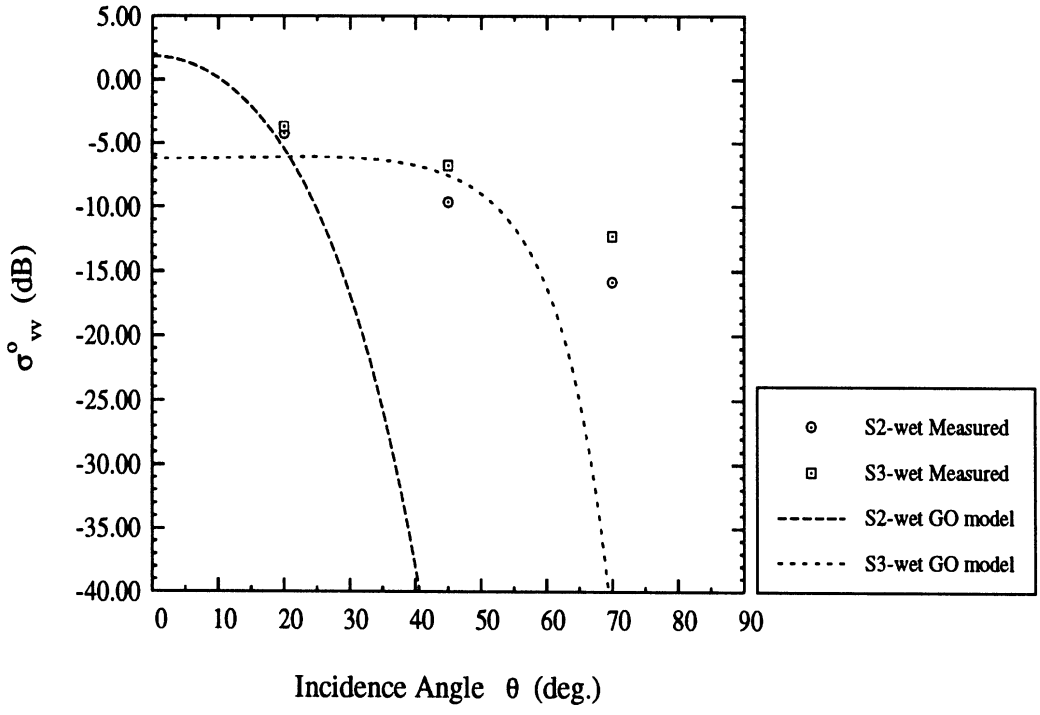

Figure B.2: Comparison between measured data and the GO model predictions at 94 GHz.

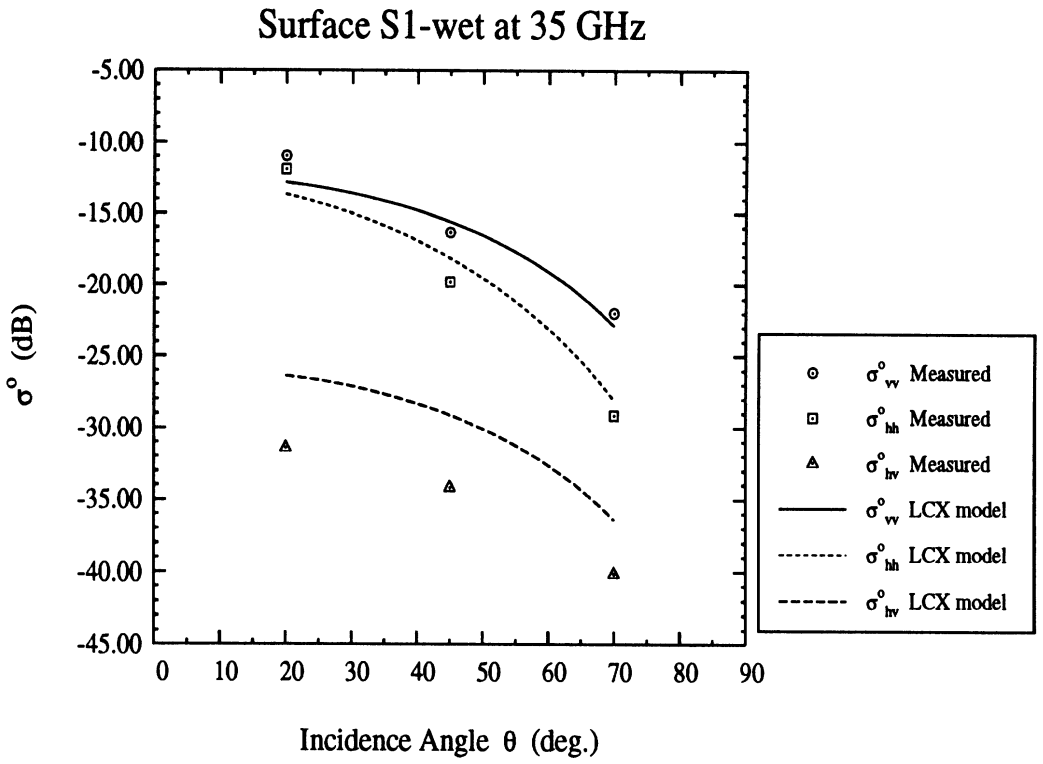

Figure B.3: Comparison between measured data at 35 GHz for S1-wet soil surface and the predictions of the LCX empirical model.

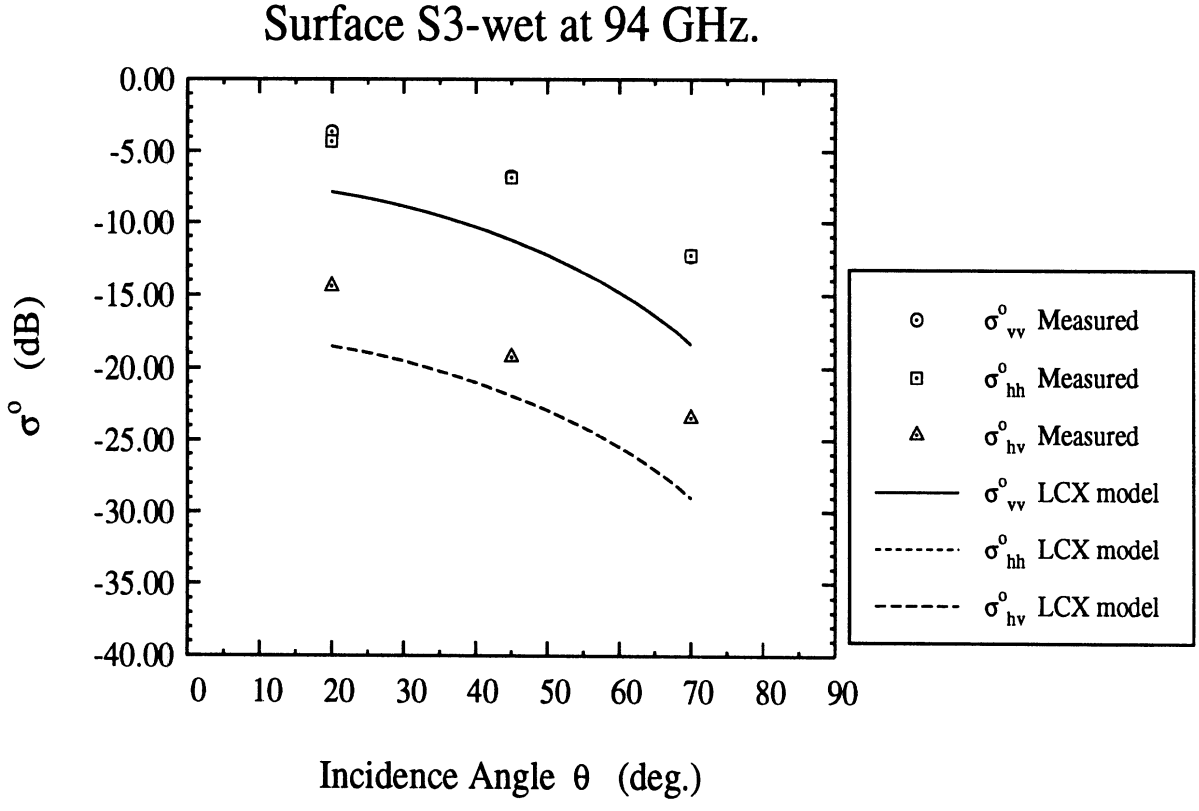

Figure B.4: Comparison between measured data at 94 GHz for S3-wet soil surface and the predictions of the LCX empirical model.

APPENDIX C

Modeling The Volume-Scattering Contribution From The Soil Medium At Millimeter Wavelengths

The soil medium is modeled as a thin dry soil layer of thickness d, comprised of air voids (acting as scatterers) imbedded in solid soil (acting as background) overlying a wet soil half space, as shown in Fig. C.1. By assuming the radius of curvature of the gently undulating air-soil interface to be large compared to the wavelength, the boundary of the thin layer can then be approximated by a tangential smooth surface at every point on the surface. This implies that the volume scattering from any point within the thin soil layer can be attributed mainly to the incident field on the nearby soil surface. The volume scattering is computed by solving the radiative transfer equation numerically with the local incidence angle determined from the unit vector along the direction of propagation and the surface normal unit vector. The total volume scattering is computed from the incoherent addition of the volume scattering contributions emerging from all points on the surface, each weighted by the probability of occurance of its surface normal. This approach is similar to that reported in [8] for computing surface scattering from tilted perturbed planes.

C.1 Volume Scattering from an Undulating Soil Surface

Consider the geometry shown in Fig. C.2 with the unit vector $\hat{n}$ representing the normal to the random rough surface, defined as

$$\hat{n} = \cos\phi_t \sin\theta_t \hat{x} + \sin\phi_t \sin\theta_t \hat{y} + \cos\theta_t \hat{z} \tag{C.1}$$

and the unit vectors $\hat{k}_i$ and $\hat{k}_s$ representing the incident and scattered directions, respectively. Following the backscatter alignment (BSA) convention defined in [5], we let ($\hat{v}_i$, $\hat{h}_i$) and ($\hat{v}_s$, $\hat{h}_s$) denote the unit polarization vectors for the incident and scattered fields, respectively. The unit vectors ($\hat{k}_i$, $\hat{v}_i$, $\hat{h}_i$) representing the incident field can be expressed in terms of the incidence angles (θ_i, ϕ_i) as

$$\begin{aligned} \hat{k}_i &= \cos\phi_i \sin\theta_i \hat{x} + \sin\phi_i \sin\theta_i \hat{y} + \cos\theta_i \hat{z} \\ \hat{h}_i &= \frac{\hat{z} \times \hat{k}_i}{|\hat{z} \times \hat{k}_i|} \\ \hat{v}_i &= \hat{h}_i \times \hat{k}_i \end{aligned} \tag{C.2}$$

similarily, the unit vectors ($\hat{k}_s$, $\hat{v}_s$, $\hat{h}_s$) representing the scattered field can be expressed in terms of the scattering angles (θ_s, ϕ_s) as

$$\begin{aligned} \hat{k}_s &= -[\cos\phi_s \sin\theta_s \hat{x} + \sin\phi_s \sin\theta_s \hat{y} + \cos\theta_s \hat{z}] \\ \hat{h}_s &= \frac{\hat{z} \times \hat{k}_s}{|\hat{z} \times \hat{k}_s|} \\ \hat{v}_s &= \hat{h}_s \times \hat{k}_s \end{aligned} \tag{C.3}$$

The local angle of incidence θ_1 can be determined for any point on the surface from $\cos\theta_1 = -\hat{k}_i.\hat{n}$ and similarly, the local scattering angle θ_2 can be determined from $\cos\theta_2 = -\hat{k}_s.\hat{n}$ in which both angles θ_1 and θ_2 are functions of θ_t and ϕ_t which in turn define the local surface normal $\hat{n}$.

Moreover, the unit polarization vectors can be defined in the local frame of reference of any point on the random surface using the following relations

$$\begin{aligned} \hat{h'}_i &= \frac{\hat{k}_i \times \hat{n}}{|\hat{k}_i \times \hat{n}|} \\ \hat{v'}_i &= \hat{k}_i \times \hat{h'}_i \end{aligned} \tag{C.4}$$

and

$$\hat{h'}_s = \frac{\hat{k}_s \times \hat{n}}{|\hat{k}_s \times \hat{n}|} \tag{C.5}$$

$$\hat{v'}_s = \hat{k}_s \times \hat{h'}_s$$

In the backscatter direction ($\theta_s = \pi - \theta_i$, $\phi_s = \pi + \phi_i$ leading to $\hat{k}_i = \hat{k}_s$, $\hat{v}_i = \hat{v}_s$, $\hat{h}_i = \hat{h}_s$ and $\theta_1 = \theta_2$) the scattering amplitudes in the global frame of reference ($\hat{k}_s$, $\hat{v}_s$, $\hat{h}_s$) can be related to those in the local frame of reference ($\hat{k}_s$, $\hat{v'}_s$, $\hat{h'}_s$) *via* simple coordinate transformations that can be put in matrix form

$$\bar{\mathbf{S}} = \bar{\bar{\mathbf{T}}}\ \bar{\mathbf{S}}' \tag{C.6}$$

where

$$\bar{\mathbf{S}} = \begin{bmatrix} s_{vv} \\ s_{hv} \\ s_{hh} \end{bmatrix} \quad , \quad \bar{\mathbf{S}}' = \begin{bmatrix} s'_{vv} \\ s'_{hv} \\ s'_{hh} \end{bmatrix} \tag{C.7}$$

s_{ij} and s'_{ij} $(i, j = v, or\ h)$ are the scattering amplitudes in the global and local frame of reference, respectively, and $\bar{\bar{\mathbf{T}}}$ is the coordinate transformation matrix

$$\bar{\bar{\mathbf{T}}} = \begin{bmatrix} (\hat{v}_s.\hat{v'}_s)^2 & 2\,(\hat{v}_s.\hat{v'}_s)(\hat{v}_s.\hat{h'}_s) & (\hat{v}_s.\hat{h'}_s)^2 \\ (\hat{v}_s.\hat{v'}_s)(\hat{v'}_s.\hat{h}_s) & (\hat{v}_s.\hat{v'}_s)(\hat{h}_s.\hat{h'}_s) + (\hat{v}_s.\hat{h'}_s)(\hat{h}_s.\hat{v'}_s) & (\hat{h}_s.\hat{h'}_s)(\hat{v}_s.\hat{h'}_s) \\ (\hat{h}_s.\hat{v'}_s)^2 & 2\,(\hat{h}_s.\hat{h'}_s)(\hat{h}_s.\hat{v'}_s) & (\hat{h}_s.\hat{h'}_s)^2 \end{bmatrix} \tag{C.8}$$

Upon multiplying $\bar{\mathbf{S}}$ with $\bar{\mathbf{S}}^{*\mathbf{t}}$ (where $*$ refers to the complex conjugate and t refers to the transpose of a matrix) and taking the ensumble average (<>), we obtain

$$< \bar{\bar{\mathbf{W}}} > = \int_0^{\pi/2} \int_0^{2\pi} P_{\theta_t,\phi_t}(\theta_t, \phi_t)\, \bar{\bar{\mathbf{T}}}\, \bar{\bar{\mathbf{W}}}'\, \bar{\bar{\mathbf{T}}}^{*\mathbf{t}}\, d\phi_t\, d\theta_t \tag{C.9}$$

where $\bar{\bar{\mathbf{W}}} = \bar{\mathbf{S}}\bar{\mathbf{S}}^{*\mathbf{t}}$ is the covariance matrix in the global frame of reference, $\bar{\bar{\mathbf{W}}}' = \bar{\mathbf{S}}'\bar{\mathbf{S}}'^{*\mathbf{t}}$ is the covariance matrix in the local frame of reference, and $P_{\theta_t,\phi_t}(\theta_t, \phi_t)$ is the joint probability density function of the angles (θ_t, ϕ_t) derived later on. Futhermore, the average covariance

matrix $< \bar{\bar{\mathbf{W}}} >$ can be expressed in terms of the averaged scattering amplitudes as follows:

$$< \bar{\bar{\mathbf{W}}} > = \begin{bmatrix} < |s_{vv}|^2 > & 0 & < s_{vv} s_{hh}^* > \\ 0 & < |s_{hv}|^2 > & 0 \\ < s_{hh} s_{vv}^* > & 0 & < |s_{hh}|^2 > \end{bmatrix} \tag{C.10}$$

In should be noted that:

1. The volume-scattering coefficients σ_{ij}^v $(i\ , j\ = v\ or\ h)$ are obtained directly from (C.10) by multiplying the appropriate elements with 4π.

2. The elements of matrix $\bar{\bar{\mathbf{W}}}'$ are computed for a finite set of local angles of incidence θ_1, as shown below. Then, the matrix elements are fitted to polynomials using the least square error method. These polynomials are used later in (C.9) to compute $\bar{\bar{\mathbf{W}}}$.

3. In case that $\cos\theta_1 < 0$, implying that the local angle of incidence has exceeded 90^o, we set $\bar{\bar{\mathbf{W}}}' = 0$ (this corresponds to the shadowed points on the surface).

C.2 Computation of $\bar{\bar{\mathbf{W}}}'$

To compute $\bar{\bar{\mathbf{W}}}'$ for a specified local angle of incidence θ_1, volume scattering from a thin soil layer with plane interfaces overlying a homogeneous half space of wet soil medium, shown in Fig. C.3, is computed using the radiative transfer theory.

The incoherent specific intensity vector, defined in terms of the vertical and horizontal components of the electric field (E_v, E_h)

$$\mathbf{I} = \frac{1}{\eta} \begin{bmatrix} I_v \\ I_h \\ U \\ V \end{bmatrix} = \frac{1}{\eta} \begin{bmatrix} |E_v|^2 \\ |E_h|^2 \\ 2Re(E_v E_h^*) \\ 2Im(E_v E_h^*) \end{bmatrix} \tag{C.11}$$

must satisfy the vector radiation transfer equation which governs energy propagation inside the scattering medium,

$$\frac{d\mathbf{I}(\mathbf{r},s)}{ds} = -\kappa_e \mathbf{I}(\mathbf{r},s) - \kappa_{ag}\mathbf{I}(\mathbf{r},s) + \int_{4\pi} d\Omega' \mathbf{P}(s,s')\, \mathbf{I}(\mathbf{r},s') \tag{C.12}$$

where $\mathbf{P}$ is the phase matrix for spherical particles, κ_e is the extinction due to scattering and absorption by the scatterers, and κ_{ag} is the absorption by the background medium. Explicit expressions for $\mathbf{P}$, κ_e, and κ_{ag} can be found in [5]. The exact solution of the radiative transfer equations which incorporates all orders of multiple scattering can be obtained numerically using the Gauss quadrature discrete ordinate-eigen analysis method. The details of this method can be found in [5] and [10].

In addition, the scattered specific intensity vector $\mathbf{I_s}$ can be related to the incident specific intensity vector $\mathbf{I_i}$ through the Mueller matrix, $\mathbf{M}$, as follows

$$\mathbf{I_s} = \mathbf{M}\ \mathbf{I_i} \tag{C.13}$$

where

$$\mathbf{M} = \begin{bmatrix} |s'_{vv}|^2 & |s'_{hv}|^2 & 0 & 0 \\ |s'_{hv}|^2 & |s'_{hh}|^2 & 0 & 0 \\ 0 & 0 & Re(s'_{vv}s'^{*}_{hh}) + |s'_{hv}|^2 & -Im(s'_{vv}s'^{*}_{hh}) \\ 0 & 0 & Im(s'_{vv}s'^{*}_{hh}) & Re(s'_{vv}s'^{*}_{hh}) - |s'_{hv}|^2 \end{bmatrix} \tag{C.14}$$

for an azimuthally symmetric medium.

It can be shown that the Mueller matrix elements can be obtained by solving numerically the RT equations for three incident polarizations, V, H, and 45° linear. Once the Mueller matrix elements are determined for a specific local angle of incidence θ_1, the covariance

matrix

$$\bar{\bar{\mathbf{W}}}' = \cos\theta_1 . \begin{bmatrix} |s'_{vv}|^2 & 0 & s'_{vv}s'^{*}_{hh} \\ 0 & |s'_{hv}|^2 & 0 \\ s'_{hh}s'^{*}_{vv} & 0 & |s'_{hh}|^2 \end{bmatrix} \tag{C.15}$$

is readily available.

C.3 Derivation of $P_{\theta_t,\phi_t}(\theta_t, \phi_t)$

For most natural surfaces, the surface height $z(x,y)$ is a stationary Gaussian random process with zero mean and variance s^2, and an autocorrelation function ρ. It can be shown that the surface slopes Z_x and Z_y along x and y respectively are normal and independent random processes with their joint probability density function given by

$$P_{Z_x,Z_y}(Z_x, Z_y) = \frac{1}{2\pi m^2} exp(-[Z_x^2 + Z_y^2]/2m^2) \tag{C.16}$$

where the variance is given by $m^2 = s^2\rho''(0)$. For a Gaussian surface auto-correlation function with a correlation length l, the rms slope becomes $m = \sqrt{2}\, s/l$.

To derive the joint probability density function of the angles θ_t and ϕ_t, we need first to relate these angles to the surface slopes, Z_x and Z_y. This can be accomplished by realizing that the unit vector representing the surface normal $\hat{n}$ can be expressed in terms of the surface slopes as follows

$$\hat{n} = (-Z_x\,\hat{x} - Z_y\,\hat{y} + \hat{z})\,D_o \tag{C.17}$$

with $D_o = 1/\sqrt{1 + Z_x^2 + Z_y^2}$

From equations (C.1) and (C.17), the surface slopes could be related to the angles (θ_t, ϕ_t) as follows

$$\cos\phi_t \sin\theta_t = -Z_x D_o$$

$$\sin\phi_t \sin\theta_t = -Z_y D_o$$

$$\cos\theta_t = D_o$$

which can be rearranged in the following form

$$\begin{aligned} Z_x &= -\frac{\cos\phi_t \sin\theta_t}{\cos\theta_t} \\ Z_y &= -\frac{\sin\phi_t \sin\theta_t}{\cos\theta_t} \end{aligned} \tag{C.18}$$

Then, it is straight forward to show that the joint probability density function for the angles (θ_t, ϕ_t) is

$$P_{\theta_t,\phi_t}(\theta_t, \phi_t) = \frac{1}{2\pi m^2} \frac{\tan\theta_t}{\cos^2\theta_t} exp(-\tan^2\theta_t/2m^2) \tag{C.19}$$

More specifically, the marginal probability density function of θ_t can be easily derived from (C.19)

$$P_{\theta_t}(\theta_t) = \frac{1}{m^2} \frac{\tan\theta_t}{\cos^2\theta_t} exp(-\tan^2\theta_t/2m^2) \tag{C.20}$$

which is plotted in Fig. C.4 for different values of m.

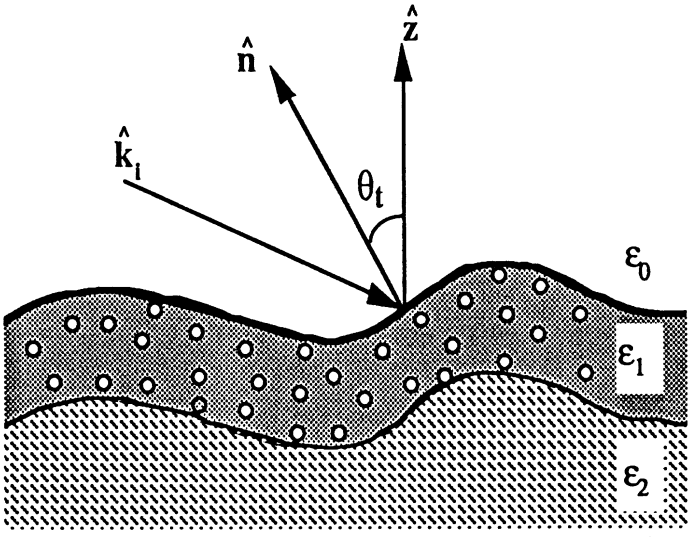

Figure C.1: Proposed model for the dry soil medium.

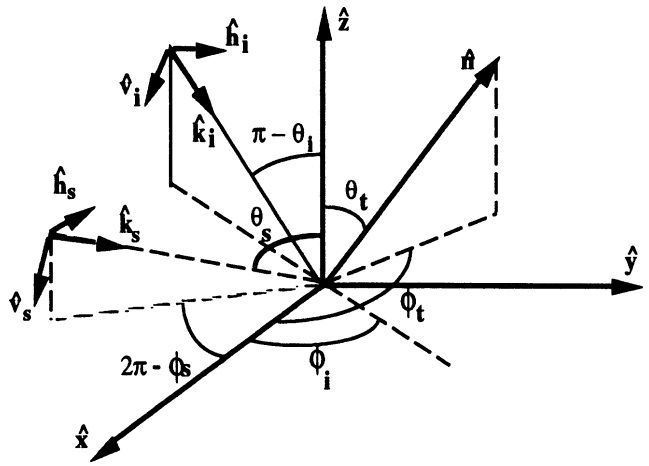

Figure C.2: Backscattering alignment (BSA) convention.

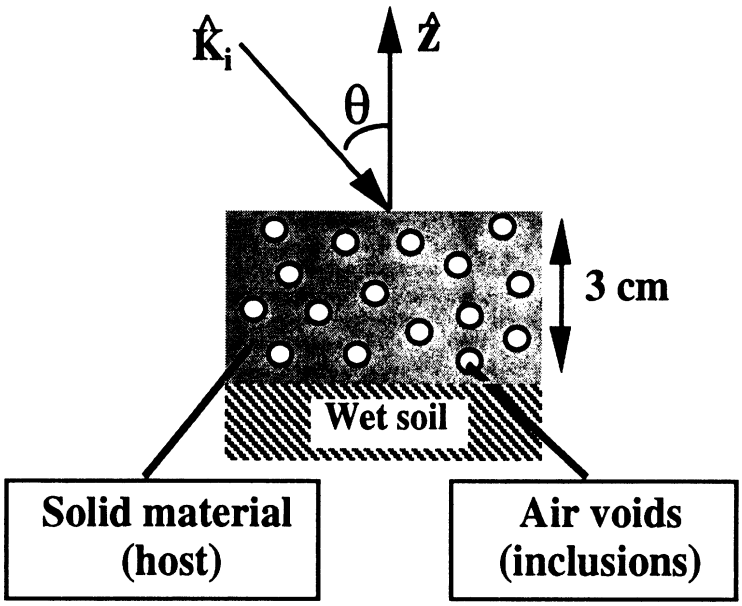

Figure C.3: A Scattering layer overlying a homogeneous half space dielectric with planar interfaces.

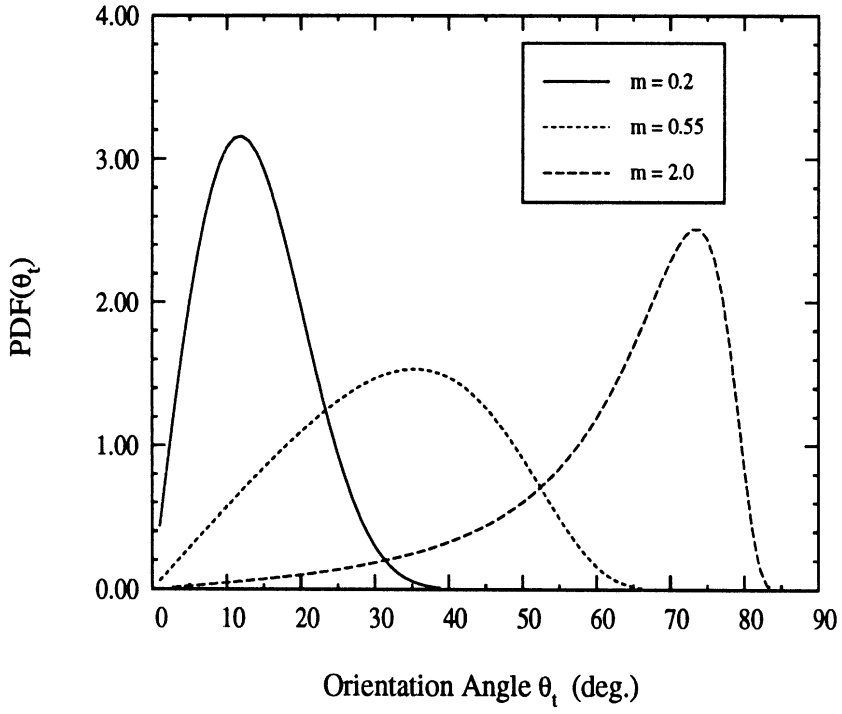

Figure C.4: The marginal probability density function $P_{\theta_t}(\theta_t)$ for different values of the rms slope m.